Measuring the Submillimeter Dust Emission from Hot Molecular Cores
Testing a Fourier Transform Spectrometer for the Submillimeter

by
Rachel Katherine Friesen
B.Sc.H., Queen's University, 2002

A Thesis Submitted in Partial Fulfillment of the
Requirements for the Degree of
MASTER OF SCIENCE
in the Department of Physics and Astronomy

Supervisor: Dr. D. Johnstone

Abstract

A Fourier Transform Spectrometer on the James Clerk Maxwell Telescope is used to study the submillimetre continuum emission from dust in three hot molecular cores (HMCs). The spectral index β of the dust emission from three sources has been determined solely within the 30 GHz wide 850μm passband to an accuracy comparable to those determined through multi-wavelength observations. We find an average $\beta \simeq 2.3$, in agreement with spectral indices determined from previous submillimetre observations of these sources and with those determined for HMCs in general. The largest single source of uncertainty in these results is the variability of the atmosphere at 850μm, and with better sky subtraction techniques we show that the dust spectral index can clearly be determined within one passband to high accuracy using a submillimetre FTS. With these results, we provide estimates of the source brightnesses required to determine the spectral index of dust emission using an imaging FTS on SCUBA-2, the next generation wide-field submillimetre camera currently under development to replace the existing SCUBA detecter at the JCMT in 2006. An imaging FTS will provide spectral information at every pixel in the field of view simultaneously at 450 and 850μm, allowing measurements of the variations in dust properties across molecular clouds and cores. The design of the imaging FTS enables instantaneous background sky emission subtraction. Combined with the new SCUBA-2 detectors, this will provide per pixel sensitivities $\sim$ 100 times greater than the FTS used in this study.

Table of Contents

List of Tables

List of Figures

Acknowledgements

There are many people who have helped and inspired me on the path to the place where I am now. Here, I would like to send a few of them my thanks and gratitude, and hope that in some way I can pass on the many lessons I've learned to those I meet in turn.

...to my supervisor, Doug Johnstone, for his guidance and confidence, and for sharing with me both his knowledge and vast enthusiasm.

...to David Naylor and the FTS group at Lethbridge, for providing the instrument used in this thesis as well as their expertise in all matters FTS.

...to Gary Davis, for the data reduction software and use of his personal time on the James Clerk Maxwell Telescope for this study, and to Caroline for inviting us into their home for wonderful after-observing run barbecues.

...to Brigitte Hesman, for her ever-ready responses to all my questions even when in the middle of her own work, and for being a fabulous partner for exploring the Big Island.

...to the friends I've made in the places I've been, both old and new, for conversation and drinks and music and laughter.

...to my family, Mom and Dad and Laura and Phil, and to my grandparents, aunts, uncles and cousins, for their unconditional love and support even when I decided to study dust in space when I could quite easily (and cheaply!) study the dust under my bed.

...and to Greg, for travelling with me through frustrations and exhilarations, for providing both an attentive ear and an encouraging voice, and for being my loving partner on this journey.

Chapter 1

Introduction

1.1 Dust in Star Forming Regions

Stars form in dense cores of dust and gas within molecular clouds, but remain cocooned in the material of their natal envelopes. Though young stars and protostars can be extremely luminous, the enveloping dust absorbs nearly all of the ultraviolet and optical starlight and reradiates it at longer wavelengths. As can be seen in Figure 1.1, we are therefore unable to probe the interiors of most dense star forming regions at optical wavelengths, and to study them we need to observe their continuum emission from dust or molecular excitation line emission. In the submillimetre regime, the optical depth τ due to dust is generally much less than unity, so the dust emission is optically thin. Submillimetre observations thus sample all the dust emission within the cloud along the line of sight, and can be used to determine the column density and mass of material present (Hildebrand, 1983). Submillimetre observations of dust in star forming regions are thus frequently used to determine physical parameters of these regions. Interpretation of the observations, however, depends on the assumed dust grain temperature, composition and size distribution. The effects of composition and grain size on the dust emission are usually combined into a dust opacity, κ_ν, which can be reasonably fit empirically with a power law dependence on frequency.

At submillimetre wavelengths, dust is generally assumed to radiate as a blackbody at some average temperature T_d modified by the opacity term, κ_ν. The continuum emission from dust is then given by $S_\nu \propto \kappa_\nu B_\nu(T_d)$, where $B_\nu(T_d)$ is the Planck blackbody function at frequency ν for dust at a temperature T_d. Assuming a power law dependence on frequency, the dust opacity κ_ν can be parametrized for a given opacity κ_0 at frequency ν_0 as $\kappa_\nu = \kappa_0(\nu/\nu_0)^\beta$, where β is the spectral index of the dust emission. For optically thin emission, the dust continuum emission then follows the power law:

$$S_\nu \propto \kappa_0(\frac{\nu}{\nu_0})^\beta B_\nu(T_d) \tag{1.1}$$

The Planck function $B_\nu(T_d)$ can also be approximated as having a power-law dependence on frequency, such that $B_\nu(T_d) \propto \nu^\alpha$. Thus, $S_\nu \propto \nu^{(\beta+\alpha)} \propto \nu^\gamma$, where $\gamma = \beta + \alpha$.

Through mathematical modelling, κ_0 and β have been calculated for various dust grain shapes, compositions and size distributions (Draine and Lee, 1984; Ossenkopf and Henning, 1994; Pollack et al., 1994), which can be compared with astronomical observations. These parameters are not easily determined observationally, however, and often various combinations of the dust parameters can reproduce existing observational data with similar accuracy. Dust properties have also been observed to vary from region to region, with evidence of dust evolution along with its environment. The effect of temperature is problematic, as many regions, especially star forming cores within molecular clouds, contain dust and gas at different temperatures in their denser inner regions than in the more extended envelopes. In particular, pre-stellar cores tend to have lower temperatures in their denser, inner regions than in the surrounding envelope, while the dust around protostars is warmer in the inner core than in the outer envelope due to the radiation emitted by the central source. In addition, even dust particles in the same physical environment will not be heated similarly

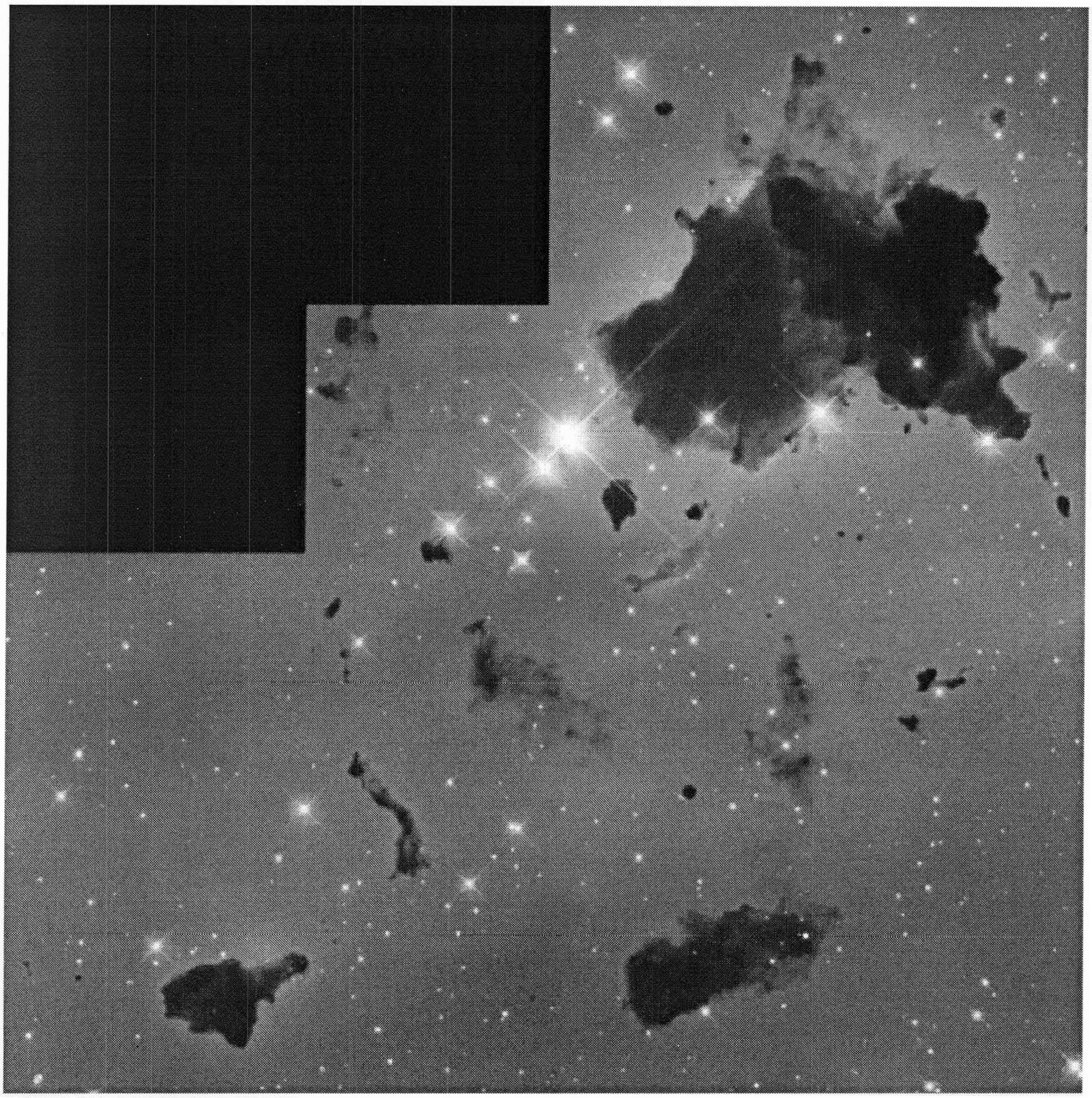

Figure 1.1 A Hubble Space Telescope Wide Field and Planetary Camera 2 optical wavelength image of Thackeray's Globules, dense dust cores where stars may be forming, in the star forming region IC 2944. It is clear that at these wavelengths, we cannot see through the dust in the denser regions of interest. Image credit: NASA and The Hubble Heritage Team (STScI/AURA)

since they are not all of the same size, and the observed column of dust will thus be composed of multiple temperature components. From Equation 1.1, the observed dust emission is strongly weighted by the dust temperature, and thus although submillimetre observations of optically thin regions sample all the dust along the line of sight, the dust is not sampled equally.

Calculations of dust temperatures and column densities based on submillimetre dust emission often assume $\beta \simeq 2$ at these wavelengths, based on work by Hildebrand (1983). In practice, however, theoretical dust grain models find spectral indices anywhere between zero and three (see the summary in Goldsmith et al., 1997), depending on the physical dust properties of the model, while observations have found a similar range of values in different states of the interstellar medium (ISM).

Inside molecular clouds, high spatial resolution observations show that dust emissivities can vary significantly on scales as small as $\sim 0.5\,\text{pc}$ (Lis et al., 1998). The spectral index β has been shown to decrease with increasing optical depth (and hence increasing column density) in the dense, cold pre-stellar cores within molecular clouds (Goldsmith et al., 1997; Visser et al., 1998; Hogerheijde and Sandell, 2000; Beuther et al., 2004), and similarly the extended envelopes around young, low mass stellar objects have been found to have higher values of β than the central peaks of the submillimetre emission (Hogerheijde and Sandell, 2000). Studies of the Orion A molecular cloud have revealed strong variations in the grain emissivity within OMC-1 (Lis et al., 1998) and some change in β across the integral shaped filament (Johnstone and Bally, 1999). Observations of the dust in circumstellar disks find a significantly lower spectral index than dust in the ISM, calculating $\beta \sim 0 - 1$ (Beckwith and Sargent, 1991). In these cold regions in general, β appears to decrease in more compact, denser objects, such that the core interiors have lower values of β than the outer envelopes.

When observing high mass star forming regions and the cores containing warmer, more evolved protostars, a different trend emerges. Williams et al. (2004) find the average frequency dependence of dust emission from > 60 high mass protostellar objects, large dense cores of dust and gas which have yet to form stars, to be $\beta = 0.9 \pm 0.4$. This is comparable to values observed in young, dense and cold objects described above, but is systematically lower than spectral indices determined through submillimetre observations of hot molecular cores (HMC) and ultra-compact HII (UCH II) regions, which are likely the next phases in the evolution of high mass protostars. In these more evolved cores, β values have been determined to be near to (Osorio et al., 1999) or slightly higher than (Hunter, 1998) ~ 2. In contrast to colder, dense objects, the dust emission from these warm, dense star-forming cores has a higher dependence on frequency.

The changing values of β in these studies are indicative of the evolution of the dust itself in the changing physical environments associated with the process of star formation. The growth of dust grains, the formation of icy mantles, and changes in grain composition are likely all significant factors in the variation of the frequency dependence of the dust emission in these regions.

A greater understanding of the properties of dust in star forming regions is needed. This requires observational methods that can discern between temperature and density effects and actual changes in the dust composition and opacity. In order to determine κ_0, observations must be calibrated against known dust column densities, which generally requires comparison with observations in shorter wavelengths. Modelling the dust greybody emission by varying the dust properties and matching predictions to observed fluxes at multiple wavelengths can place limits on the opacity and its frequency dependence and is able to provide a clearer picture of the structure and composition of the region; however the number of free parameters involved and their interdependence cause difficulties in interpretation, and obtaining data on one source at multiple frequencies can be time consuming. It is also often difficult for a single model to fit data points in the infrared and submillimetre simultaneously, although models containing multiple temperature components do better in this area than single temperature dust models.

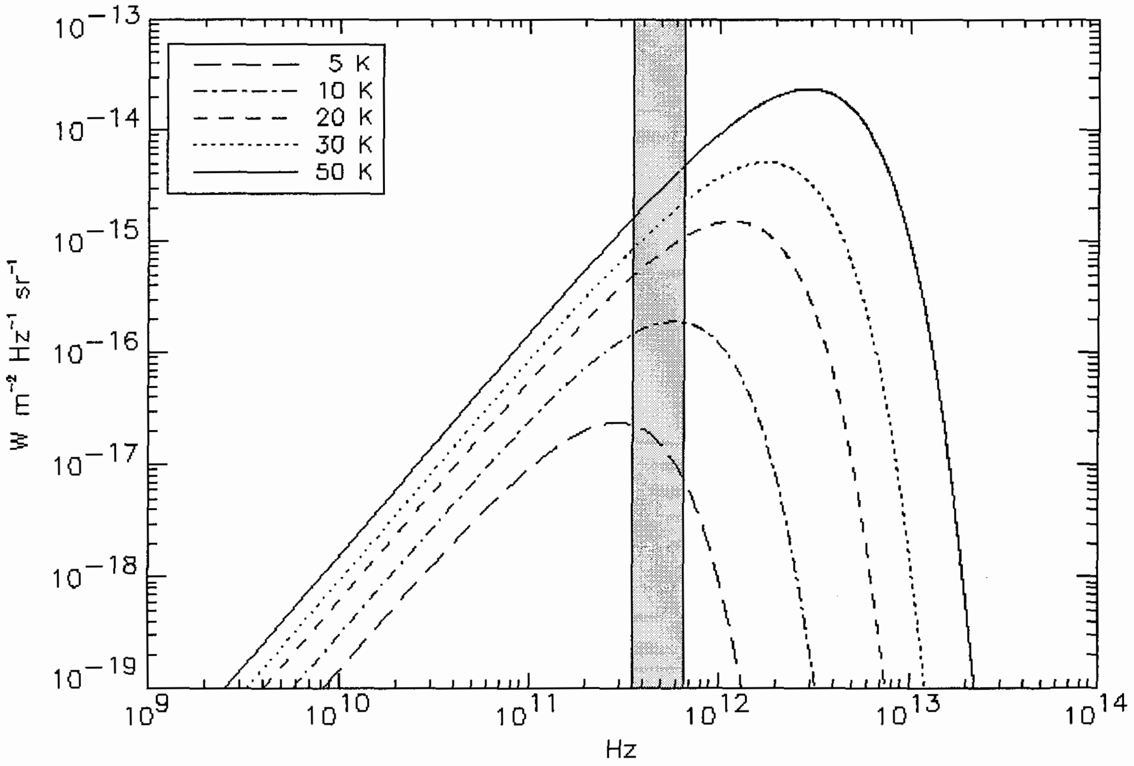

Figure 1.2 The Planck function at several temperatures typical of dust in star forming regions. The shaded area indicates the frequencies between 350 GHz and 660 GHz, which correspond to 850 μm and 450 μm respectively. Note the increased proximity of both the 450 μm and 850 μm wavelengths to the peak of the function at lower temperatures. This causes difficulties in determining the frequency dependence of the dust emission through comparison of observations at two submillimetre wavelengths (such as 450 μm and 850 μm).

In contrast, the spectral index β of the dust opacity can be calculated solely through submillimeter measurements. Traditionally, attempts to measure β have compared observations at two widely separated submillimetre wavelengths. This method provides great leverage on β, but the calculations are complicated by calibration issues from observing in the different passbands, and have the disadvantage that the value determined for β is dependent on the assumed dust temperature.

Problems arise with the larger atmospheric transmission variability at short submillimetre wavelengths, which leads to a lower signal-to-noise ratio in the observations than in those at longer wavelengths. In addition, for dust temperatures less than $\sim 40\,\mathrm{K}$, the Planck function at $450\,\mu\mathrm{m}$ is far from the Rayleigh-Jeans limit, and even at the higher temperatures expected in high mass star forming regions, for example, the change in emissivity between passbands for cold sources could be due to either small changes in temperature or large changes in the dust emissivity. The Planck function at several temperatures typical of various stages of evolution of star forming regions is plotted in Figure 1.2, showing the submillimetre regime and the increased proximity of the $450\,\mu\mathrm{m}$ window to the peak of the Planck function for sources at lower temperatures. It is extremely difficult to separate these effects without an independent measure of the dust temperature. The differences between the telescope beams at the two wavelengths also cause difficulties, as the $850\,\mu\mathrm{m}$ beam at the James Clerk Maxwell Telescope (JCMT), for example, is Gaussian with a full width half maximum of $14''$, but the beam at $450\,\mu\mathrm{m}$ has a central peak of $7''$ and extended sidelobes or pedestal caused by diffraction of the $\sim 1\,\mathrm{m}$ panels which make up the telescope dish. The relative uncertainties at the different wavelengths are much greater than ten percent due to the complicated data calibration. These complications all lead to uncertainties in the determination of β large enough that the subsequently derived physical properties of dusty systems, such as the mass estimates of the material in dense cores in molecular clouds, may range over factors of a few. For this reason, it is beneficial to observe in one passband only, as the complications are greatly reduced.

1.2 A Fourier Transform Spectrometer for the Submillimetre

One instrument that is well-suited to this problem is a Fourier Transform Spectrometer (FTS). FTS utilize the wavelike properties of light to obtain a spectrum of a light-emitting source. The typical FTS design generally uses beamsplitters to divide the incoming light, which then travels along two paths of different lengths before being recombined at another beamsplitter and sent to the detector. Information at a range of frequencies is obtained by having the length of the light travel path gradually increase through the use of translating mirrors. The detector records the produced interference pattern, or interferogram, which is then transformed using fast Fourier techniques into a spectrum. FTS have several advantages and disadvantages compared with other spectrometer designs. Their spectral resolution is limited by the length of the paths the light can travel within the instrument, which is dependent on the size of the instrument and the translation stage of the mirrors. As such, most FTS provide low to intermediate spectral resolution ($\mathrm{R}\sim 200$ - $\mathrm{R}\sim 2000 - 3000$ at 345-375 GHz, where the spectral resolution $\mathrm{R}= \nu/\delta\nu$, where $\delta\nu$ is the frequency resolution and ν is the central frequency of the bandpass), excellent for observations of sources with wide, bright spectral lines and continuum emission. For these studies FTS have a distinct advantage over high spectral resolution but narrow bandwidth heterodyne receivers. The instantaneous bandwidth of an FTS is inherently very broad, and in the submillimetre is limited only by the atmospheric transmission windows, enabling a wider spectral coverage within these windows than is possible with the heterodyne receivers currently in use.

In the past decade, two groups have successfully used FTS to study the submillimetre emission from several astronomical sources, such as the Orion molecular cloud (Serabyn and Weisstein, 1995), the Sun (Naylor et al., 2000), and the atmospheres of planets (Naylor et al., 1994; Davis et al., 1997). A submillimetre FTS operated at low resolution can sample the continuum dust emission from a source with a large enough bandwidth that the change in dust emissivity with frequency, and thus β, can be determined solely within one passband. At very low temperatures, it is still difficult to separate the temperature component of the emission from the dust power-law emissivity function, but single bandpass observations are able to place limits on the combined dust temperature and β. An FTS with high sensitivity operating at two submillimetre wavelengths (450 μm and 850 μm, for example) can determine the slope of the emission at both wavelengths and thus independently determine both the dust temperature T_d and β.

1.3 Goals of this Work

In this study, we present 850 μm dust continuum observations of four hot molecular cores obtained with a submillimetre FTS of the Mach-Zehnder design (MZ FTS) developed for use at the James Clerk Maxwell Telescope (JCMT) (Naylor et al., 2003). We describe in the following the observational procedure and analysis of the data. We compare the dust spectral index values determined for our sources with those calculated from previous submillimetre measurements, and discuss the detrimental effects of the variable submillimetre atmosphere on our sensitivity. Finally, we describe the continuum measurement capabilities of an imaging FTS currently in preparation for use at the JCMT with the new SCUBA-2 detector.

Chapter 2

Observations and Data Reduction

2.1 The Mach-Zehnder FTS

The Mach-Zehnder FTS (MZ FTS) was built for use at the James Clerk Maxwell Telescope[1] (JCMT) by the FTS group at the University of Lethbridge, AB, Canada (Naylor et al., 2003), and mounts on the right Nasmyth platform of the JCMT. The translation stage has a maximum travel of 300 mm. With the folded light path of the MZ design this provides a maximum optical path difference of 1.2 m due to the factor of four increase in the maximum light path travel length from the folded mirror design, which can be seen in Figure 2.1. This design allows the FTS to be operated at variable spectral resolution, from low resolution (0.05 cm^{-1}or 1.5 GHz, R$\sim$ 230 at 345 GHz) to intermediate resolution (0.005 cm^{-1}or 150 MHz, R$\sim$ 2300 at 345 GHz). A filter wheel is used to match the highly and uniformly efficient FTS filters with the submillimetre atmospheric transmission windows visible with the JCMT. Although the instrumental design allows the use of two detectors, only one was built for use with this FTS. The detector is a single bolometer cooled to a temperature of 0.3K

---

[1] The JCMT is operated by the Joint Astronomy Centre in Hilo, Hawaii on behalf of the parent organizations Particle Physics and Astronomy Research Council in the United Kingdom, the National Research Council of Canada and The Netherlands Organization for Scientific Research.

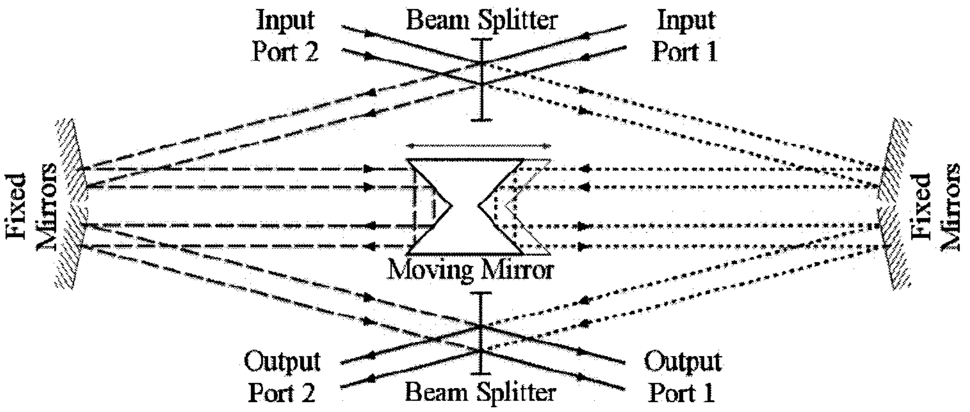

Figure 2.1 A schematic of the Mach-Zehnder FTS. In this study, Input Port 2 viewed the astronomical source while Input Port 1 viewed a cold blackbody. The detector was placed at Output Port 1. No detector was available for Output Port 1.

and is described in more detail by Naylor et al. (1999). The MZ design also enables the use of two input ports, and in this study one viewed the astronomical source while the other viewed a constant cold load (a liquid N_2 dewar).

For reference, the atmospheric radiance and transmission at 850 μm is shown in Figure 2.2 overlaid with the response function, $R(\nu)$, of the detector. The response function clearly covers the entire 850 μm transmission window. At 850 μm, the detector bandwidth is $\sim$ 30 GHz.

2.2 Observational Procedure

The observations were performed on 2003 April 21 - 28, using the MZ FTS mounted on the right Nasmyth platform of the JCMT on Mauna Kea, Hawaii. Other scheduled observing runs at the JCMT in October 2003 and March 2004 were unsuccessful for this study due to very poor, unstable weather. The April 2003 weather

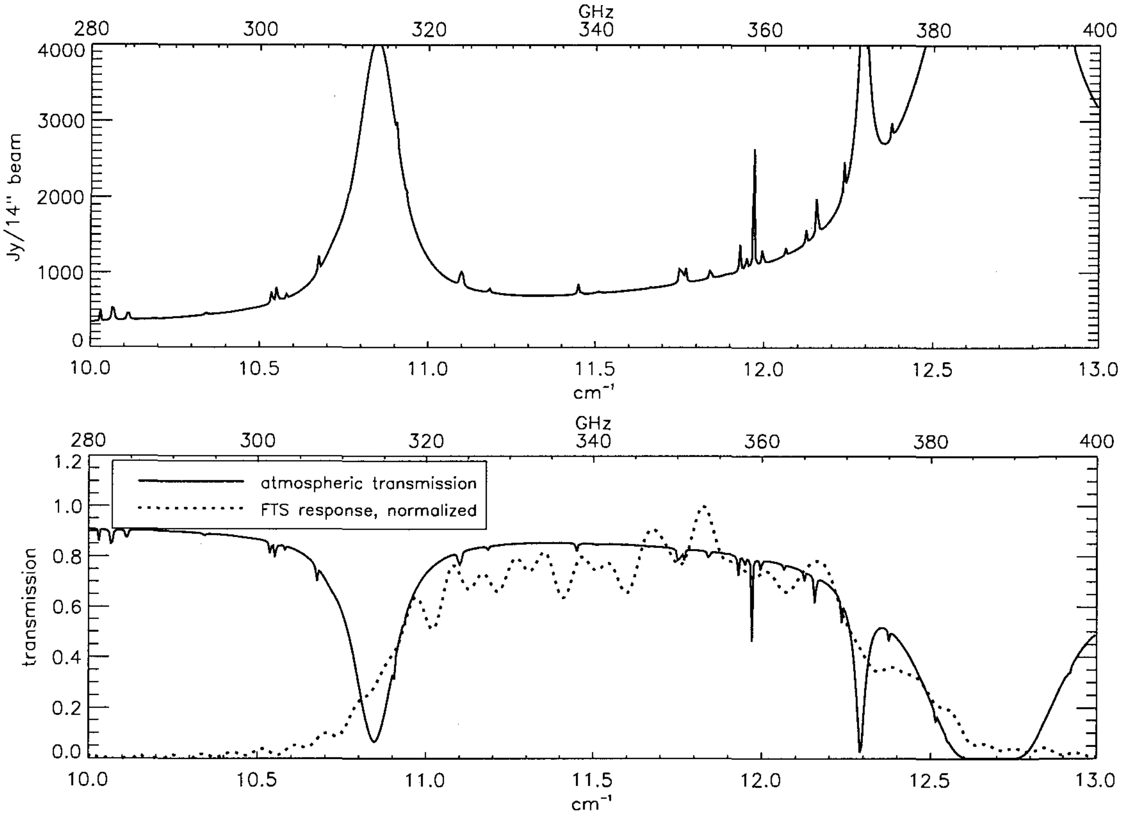

Figure 2.2 The theoretical atmospheric radiance (top) and transmission (bottom) modelled using ULTRAM for precipitable water vapour levels of 1.0 mm at Mauna Kea, similar to the average precipitable water vapour of 1.1 mm for the April 2003 observing run. The dotted line is the normalized FTS response function, $R(\nu)$.

was good to excellent with the opacity measured at 225 GHz, τ_{225}, $\sim$ 0.07 for most of the observations, giving precipitable water vapour (pwv) levels averaging $\sim$ 1.1mm. Figure 2.3 shows that there was some significant atmospheric instability at times, illustrated by jumps in the recorded precipitable water vapour levels. At 850 μm, the FTS bandwidth is $\sim$ 30 GHz. The FTS was operated at low spectral resolution (1.5 GHz or 0.05 cm^{-1}), resulting in $\sim$ 20 resolution elements across the band. The full width half maximum (FWHM) of the 850 μm beam at the JCMT is $\sim$ 14$''$, which was matched by the tunable aperture of the detector. Spectra were obtained in groups, with five spectra taken of a molecular core immediately followed by five spectra of the background sky, -1425$''$ in right ascension from the source. The offset in right ascension was calculated to compensate for the change in airmass of the source due to the Earth's rotation during the time taken to obtain five spectra, allowing the sky measurements to be taken at the same airmass as the original source observations. This is crucial for accurate background sky subtraction, as the temporal variability of the atmosphere at 850 μm is easily the largest source of uncertainty in our final results. Five scans were obtained approximately every 90 seconds, with a scan speed of 8.2 mm s^{-1}. Each source was observed for between three and four hours, with approximately half of that time spent on source and half spent on background observations. A pointing check was performed every 45 minutes.

2.3 Source Selection

The sources for this pilot study were chosen from a sample of HMC from Hatchell et al. (2000) for their large submillimetre fluxes and lack of extended structure. The sources, G10.47, G12.21, G31.41 and G43.89, have been previously studied in the submillimetre regime with the Submillimeter Common User Bolometer Array (SCUBA) at the JCMT (Hatchell et al., 2000; Walsh et al., 2003) and in the radio continuum (Wood and Churchwell (1989), among others). All four have also been detected in

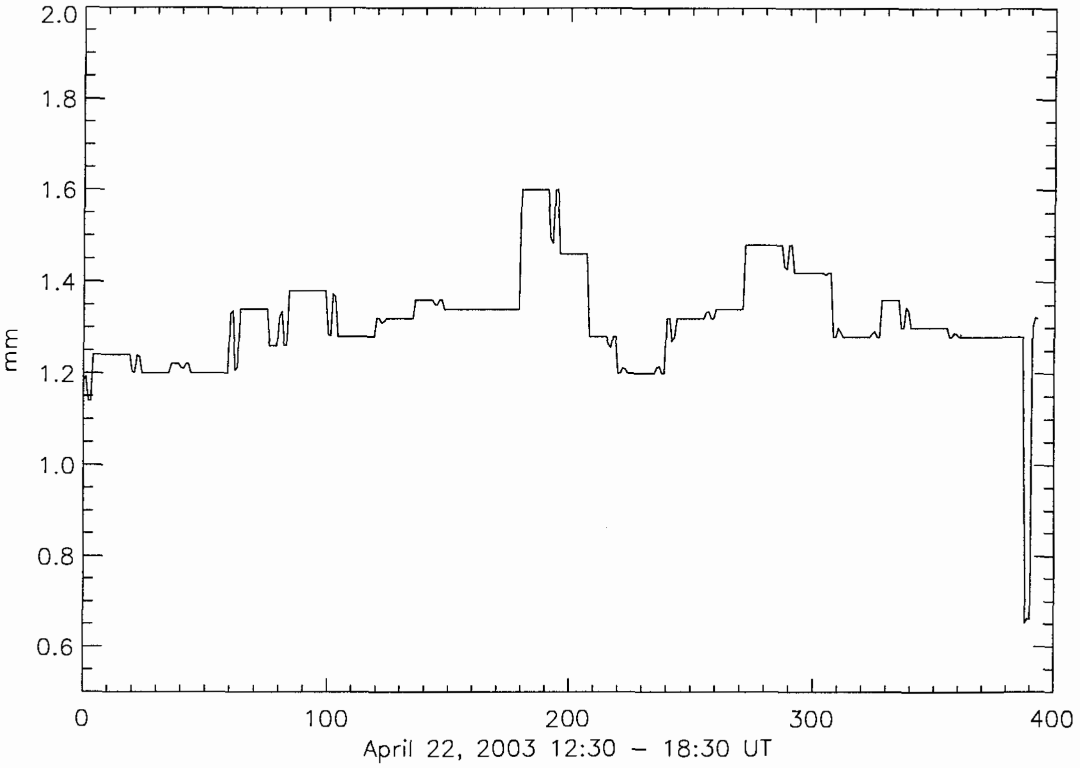

Figure 2.3 The precipitable water vapour levels at 225 GHz measured by the Caltech Submillimetre Observatory for the night of April 22, 2003.

numerous molecular lines and maser emission (see the detailed source descriptions in Hatchell et al. (2000)). Table 2.1 gives source positions and distances from Hatchell et al. (2000), and 450 μm and 850 μm peak brightnesses calculated using the archived SCUBA data[2]. Each source is associated with one or more UC H II regions near the peak of the submillimetre emission. The hot core in G10.47 alone contains three UC H II regions, G10.47-0.03A, B and C, while the other sources are coincident with one UC H II region each, G12.21-0.10, G31.41+0.31 and G43.89-0.78. Figure 2.4 shows the 850 μm SCUBA maps of all four sources. The three brighter sources are very peaked in the 850 μm emission, although G31.41 does contain some more extended emission. The actual hot cores themselves are much smaller than the JCMT beam with diameters of only 1-2$''$, whereas the G43.89 core has a size of $\sim 4''$. Core mass estimates are on the order of a few thousand $M_\odot$ (Hatchell et al., 2000). The faintest source, G43.89, was observed by us to only S/N $\sim$ 1.5, too low to analyse with any degree of certainty, and is therefore omitted from further discussion.

2.4 Data Reduction

Preliminary data reduction was performed using a processing pipeline software written in IDL for the FTS (Naylor et al., 2003). The data were first manually screened for cosmic rays, which occur approximately once in every fifteen interferograms and produce large intensity spikes at one or two data points in the interferograms. These spikes are easily detected and can be removed within the pipeline. Higher energy cosmic rays produce spikes in the interferograms over multiple data points; these interferograms were omitted from the dataset. Only a handful of interferograms were rejected for this reason. The effects of cosmic rays on the interferograms are shown in Figure 2.5. A linear phase correction was applied to the data, and the

---

[2] Guest User, Canadian Astronomy Data Centre, which is operated by the Dominion Astrophysical Observatory for the National Research Council of Canada's Herzberg Institute of Astrophysics

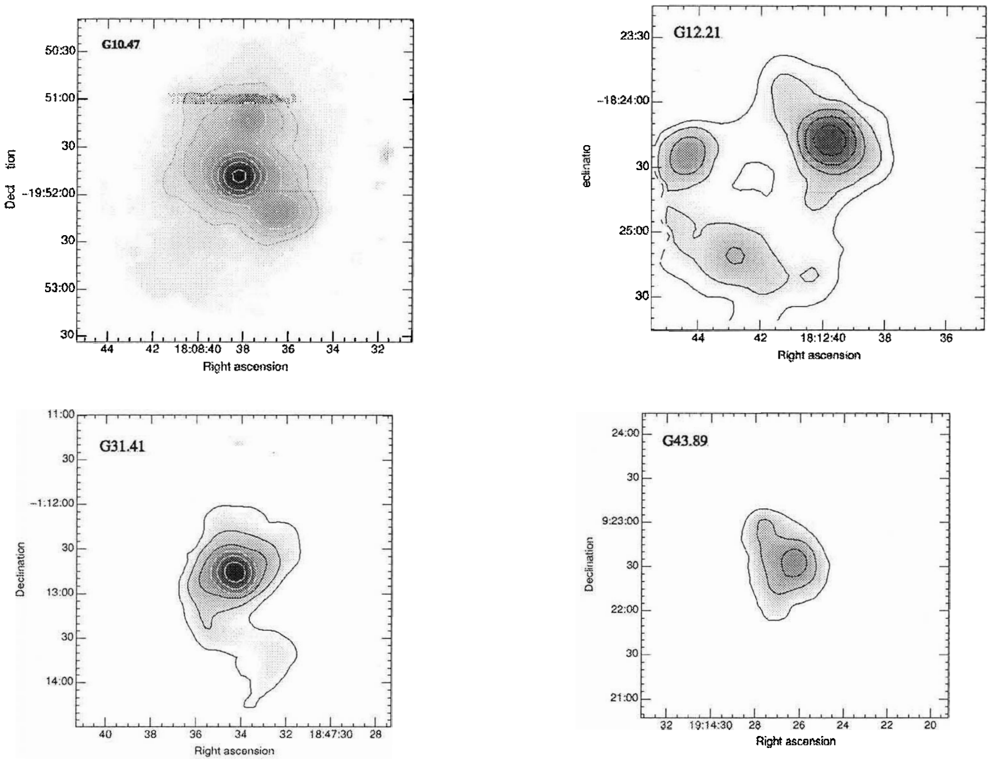

Figure 2.4 850 μm SCUBA maps of the four hot molecular cores observed in this study with the FTS. This data was taken from the JCMT archive. The contours increase in multiples of 2 from 0.5 Jy/14″ beam.

Table 2.1. Positions and peak brightnesses for observed objects

Source	α_{J2000}	δ_{J2000}	I_ν (450 μm)	I_ν (850 μm)	Distance
—	$^{\mathrm{h}}\,^{\mathrm{m}}\,^{\mathrm{s}}$	$^{\circ}\,'\,''$	Jy/9″ beam	Jy/14″ beam	kpc
G10.47	18 08 38.2	-19 51 50	260 ± 65	39.0 ± 5.9	5.8
G12.21	18 12 39.7	-18 24 20	121 ± 30	13.0 ± 2.0	13.5
G31.41	18 47 34.5	-01 12 43	130 ± 32	24.2 ± 3.6	7.9
G43.89	19 14 26.2	+09 22 34	17 ± 4.2	3.0 ± 0.4	4.2

Note. — The positions, peak brightnesses at 450 μm and 850 μm, and distances to each of the hot molecular cores observed in this study. Positions and distances are taken from Hatchell et al. (2000), while peak brightnesses were calculated from the archived SCUBA data.

individual interferograms were Fourier transformed, both unapodized and using different apodization functions. The abrupt cut-off of a truncated interferogram causes a phenomenon known as 'ringing'. The finite travel length of the translation stage in any FTS means that all measured interferograms are truncated and thus contain ringing effects. An apodization function is a mathematical function used to bring the interferogram smoothly to zero at the ends of the data, which reduces the ringing at the expense of a decrease in the spectral resolution. The usefulness and effects on the analysis of using an apodization function in this analysis will be discussed in more detail in Chapter 3.

After Fourier transforming the interferograms, the spectra were then coadded into the on- and off-source groups of five, and the coadded off-source background scans were then subtracted from the coadded on-source scans. Each background-subtracted spectrum was then corrected for atmospheric transmission within the band using an atmospheric transmission model described in Davis et al. (1997). The atmospheric transmission model parametrizes the atmospheric transmittance in terms of the pwv and airmass, and includes H_2O (water vapour), O_3 (ozone) and O_2 (molecular oxygen) as atmospheric absorbers. In this study, an updated coefficient file calculated with the University of Lethbridge Transmission and Radiance Atmospheric Model (ULTRAM) (Chapman, 2000) was used with the model by Davis et al. (1997). ULTRAM is a radiative transfer atmospheric model which calculates the radiance and transmission of the atmosphere through a line-by-line, layer-by-layer analysis, and was written with the specific goal of accurately modelling the atmosphere above Mauna Kea. The airmass of each scan was recorded with each interferogram. The opacity at 225 GHz, τ_{225}, was recorded by the Caltech Submillimetre Observatory (CSO). The use of this opacity value in the data analysis likely introduces some uncertainty into the final results, as the CSO radiometer operates at a fixed azimuth and only updates approximately every twenty minutes, while the pwv levels in the atmosphere vary significantly on shorter timescales. This can be seen in Figure 2.6, where τ_{225} from

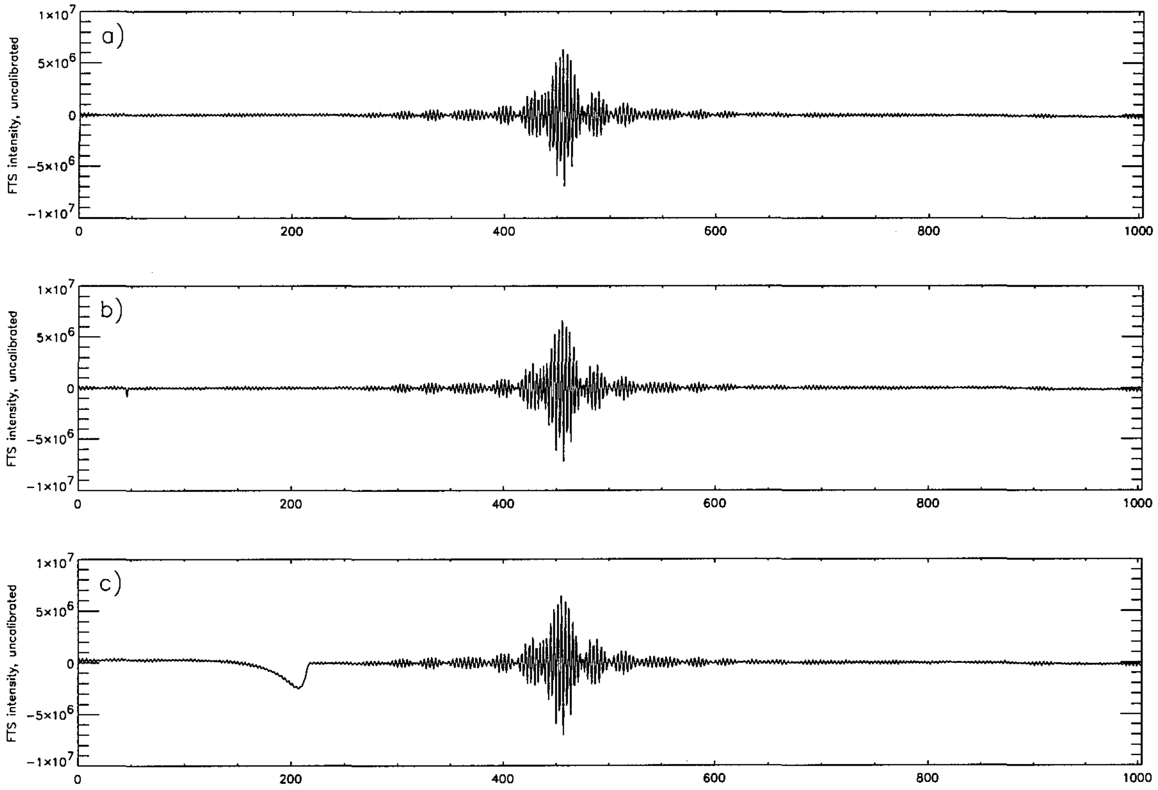

Figure 2.5 The effect of cosmic rays on the interferograms. An interferogram without any cosmic ray effects is shown in a). A cosmic ray has hit the detector in plot b), but this is a small spike that can be cleaned up within the data reduction pipeline. A larger energy ray has hit the detector in c), and this interferogram had to be taken out of the final data set.

the CSO is plotted against τ_{225} determined from measurements of the pwv recorded by the JCMT's water vapour monitor for a twenty minute period during the observations of G10.47. The CSO τ_{225} does not reflect the short timescale of the opacity variability. Since each scan takes only 8 s to complete, however, these opacity variations should have a small impact on our results.

The FTS response, like a filter function, was determined through observations of calibrator blackbodies at two temperatures placed in the FTS input port, and was removed from the coadded spectrum to produce the final low resolution 850 μm spectrum for each source.

In an attempt to increase the final S/N ratio achieved for each source, the individual spectra were compared with the final mean spectrum and ordered in degree of spread from the mean. This ordering was done by only comparing points well within the bandpass, as the atmospheric corrections tend to increase the noise at the edges of the band where the atmospheric transmission becomes very small. Those spectra whose points across the band were far, on average, from the mean (of order 3 standard deviations) were removed from the dataset and the remaining spectra were again coadded to produce a new mean spectrum. Figure 2.7 shows the results of the data removal for G10.47. The number of outlying spectra comprised only a small portion of the total dataset (approximately 5% of the total number of scans for each source), and the removal of these spectra with large deviations from the mean did not significantly affect the signal strength or the S/N ratio of the final coadded spectrum. All further analysis was then done using all the data available.

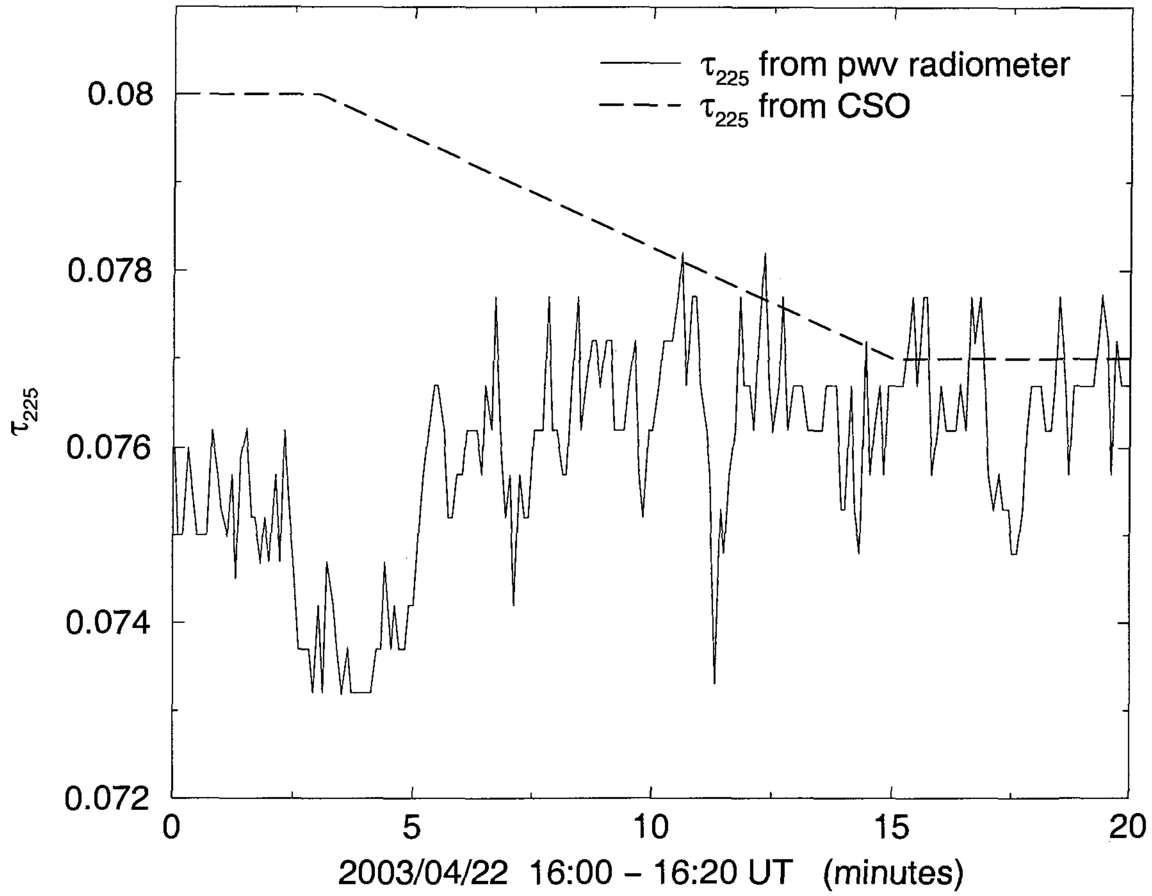

Figure 2.6 The opacity measured from the CSO and determined through measurements of the pwv by the JCMT's water vapour monitor for a 20 minute period during observations of G10.47. The short timescale opacity variations are not captured by the measurements made every 15-20 minutes at the CSO.

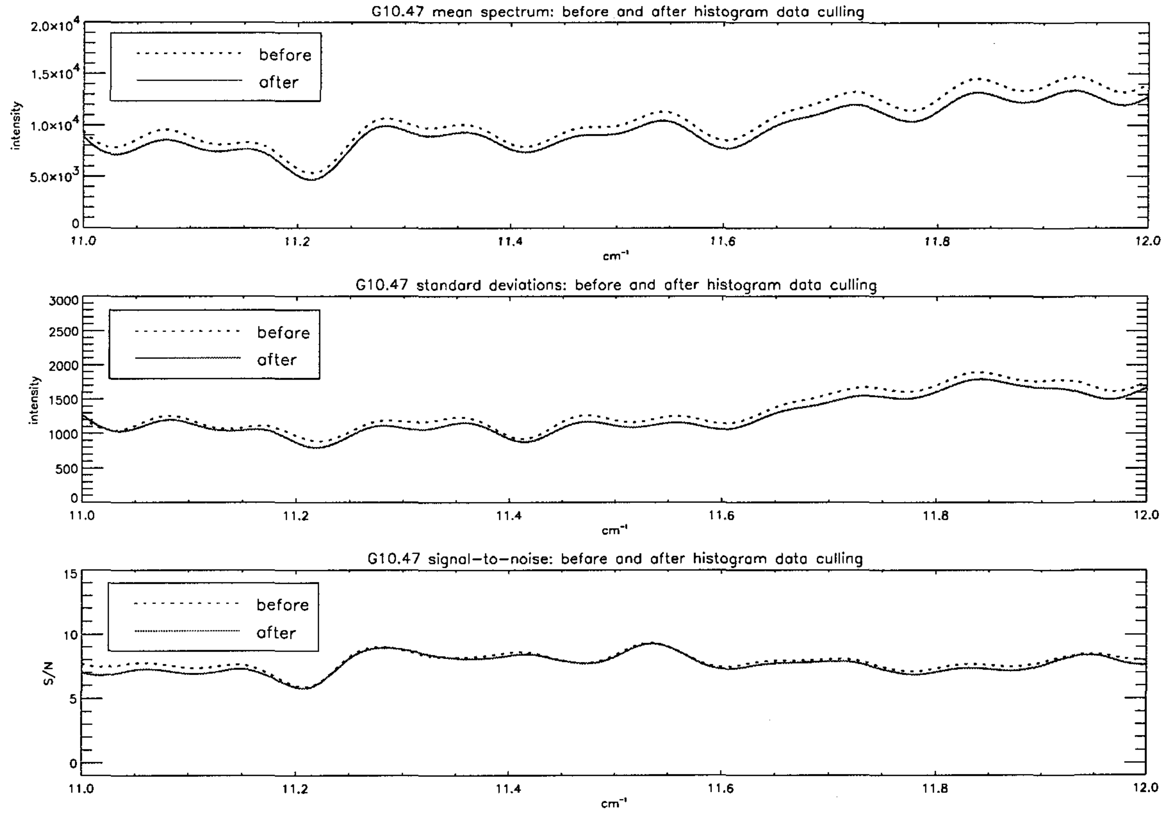
G10.47 mean spectrum: before and after histogram data culling

G10.47 standard deviations: before and after histogram data culling

G10.47 signal-to-noise: before and after histogram data culling

Figure 2.7 The effect on the signal strength and standard deviation per point for the final spectrum of G10.47 of culling from the data set those spectra with extreme deviations from the mean. For each source, the overall S/N remained unchanged.

Chapter 3

Analysis

3.1 Source signal analysis

The measured signal S as a function of frequency ν from an astronomical source through the FTS can be expressed as

$$S(\nu) = R(\nu)\, G\, [\eta_a\, J_s(\nu)\, \mathrm{e}^{-\tau(\nu)} + \eta_a\, J_{sky}(\nu)(1 - \mathrm{e}^{-\tau(\nu)}) + (1 - \eta_a)\, J_{amb}(\nu) - J'(\nu)] \quad (3.1)$$

Here, $\tau(\nu)$ is the atmospheric optical depth as a function of frequency ν, the telescope aperture efficiency is given by η_a, and G is the detector gain when observing an astronomical source. For the hot core observations, the gain was set to $G = 10^4$. These calculations were performed assuming the telescope efficiency $\eta_a = 0.56$ for the FTS. This value is the telescope efficiency for SCUBA, which operates at the JCMT through the same optics up to the telescope's tertiary mirror, and at the same wavelength, as the FTS. This value should therefore be a good approximation; however we note that the efficiency for the FTS has not been measured. $J_s(\nu)$ is the true spectrum of the source, $J_{sky}(\nu)$ is the true spectrum of the atmosphere, $J_{amb}(\nu)$ is the power received from ambient temperature surfaces of the telescope, and $J'(\nu)$ is the power received through the 2^{nd} port of the FTS, which is differenced in the interferometric measurement (Naylor et al., 2000). The first term therefore represents the power received from the astronomical source itself through the atmosphere and instrument, the second term represents the power received from the atmosphere and the third term represents the power received from the surfaces of the telescope, which are at ambient temperature. $R(\nu)$ is the responsivity or response function of the FTS (shown in Figure 2.2) and is determined by placing warm and ambient blackbody sources in one input port of the FTS:

$$\begin{aligned} S_{warm} &= G'\,R(\nu)\,[\,B(\nu,T_{warm}) + (1-\eta_a)\,J_{amb}(\nu) - J'(\nu)] \\ S_{amb} &= G'\,R(\nu)\,[\,B(\nu,T_{amb}) + (1-\eta_a)\,J_{amb}(\nu) - J'(\nu)] \\ S_{warm} - S_{amb} &= G'\,R(\nu)\,[B(\nu,T_{warm}) - B(\nu,T_{amb})] \end{aligned}$$

$$R(\nu) = \frac{S_{warm}(\nu) - S_{amb}(\nu)}{G'\,[B(\nu,T_{warm}) - B(\nu,T_{amb})]} \qquad (3.2)$$

$S_{warm}(\nu)$ and $S_{amb}(\nu)$ are the observed warm and ambient blackbody spectra, respectively, while $B(\nu,T_{warm})$ and $B(\nu,T_{amb})$ are the respective Planck blackbody functions. When viewing the blackbody source, the detector gain G' was set to 10^3. Here, we are assuming that the atmospheric absorption between the blackbody and the detector is negligible. Observations at the background position produce solely the intensity received from the sky, $S_{sky}(\nu)$:

$$S_{sky}(\nu) = G\,R(\nu)\,[\eta_a\,J_{sky}(\nu)(1-\mathrm{e}^{-\tau(\nu)}) + (1-\eta_a)J_{amb}(\nu) - J'(\nu)] \qquad (3.3)$$

If the atmospheric temperature and opacity are assumed to remain unchanged during each pair of source and background scans, the difference of the on- and off-source scans gives the observed power of the source itself, $S_s(\nu)$:

$$S_s(\nu) = S(\nu) - S_{sky}(\nu) = R(\nu)\,G\,\eta_a\,J_s(\nu)\,\mathrm{e}^{-\tau(\nu)} \qquad (3.4)$$

Sky brightnesses for the typical pwv levels during our observations of $\sim$ 1.1 mm at 345 GHz are $\sim$ 730 Jy/14″ beam, an order of magnitude larger than our brightest source, making accurate background subtraction essential. During the observations, measurements of the precipitable water vapour, from the CSO radiometer, and observational airmass were recorded. With this information, the atmospheric model described in Chapter 2 was used to determine the transmission of the atmosphere in the direction of the source, and thus the contribution of the term $e^{-\tau(\nu)}$ to the observed source intensity $S_s(\nu)$. Typical values of τ_{225} during the observations were ~ 0.07, leading to atmospheric transmission levels at 345 GHz of $\sim 70\%$ (calculated using the relation between τ_{225} and the pwv from Davis et al. (1997), and the relationship between the pwv and the opacity at 345 GHz, τ_{345}, determined by Chapman et al. (2004)). With these corrections, the true spectrum $J_s(\nu)$ of the astronomical source can then be calculated:

$$J_s(\nu) = \frac{S_s(\nu)}{G\,R(\nu)\,\eta_a\,e^{-\tau(\nu)}} \tag{3.5}$$

The final 850 μm spectrum of each source can be seen in Figures 3.1-3.3. The discontinuities at the edges of the band are caused by the application of the transmission correction only within the bandpass, and are artificial. The transmission in the 850 μm window drops rapidly at the edges of the FTS band. Although the source signal is very small in these regions, the smaller transmission values cause a large rise in the flux when dividing the signal by $e^{-\tau(\nu)}$. Since the atmospheric corrections were applied after Fourier transformation, this results in very sharp edges to the spectra.

3.2 Signal-to-noise and atmospheric effects

The instrumental signal-to-noise (S/N) was calculated from the MZ FTS characteristics in Naylor et al. (2003) for the spectral resolution and specific observing times for each source, and is solely due to the detector noise of the FTS. The S/N of the final spectra are compared with the instrumental S/N in Table 3.1, with the average

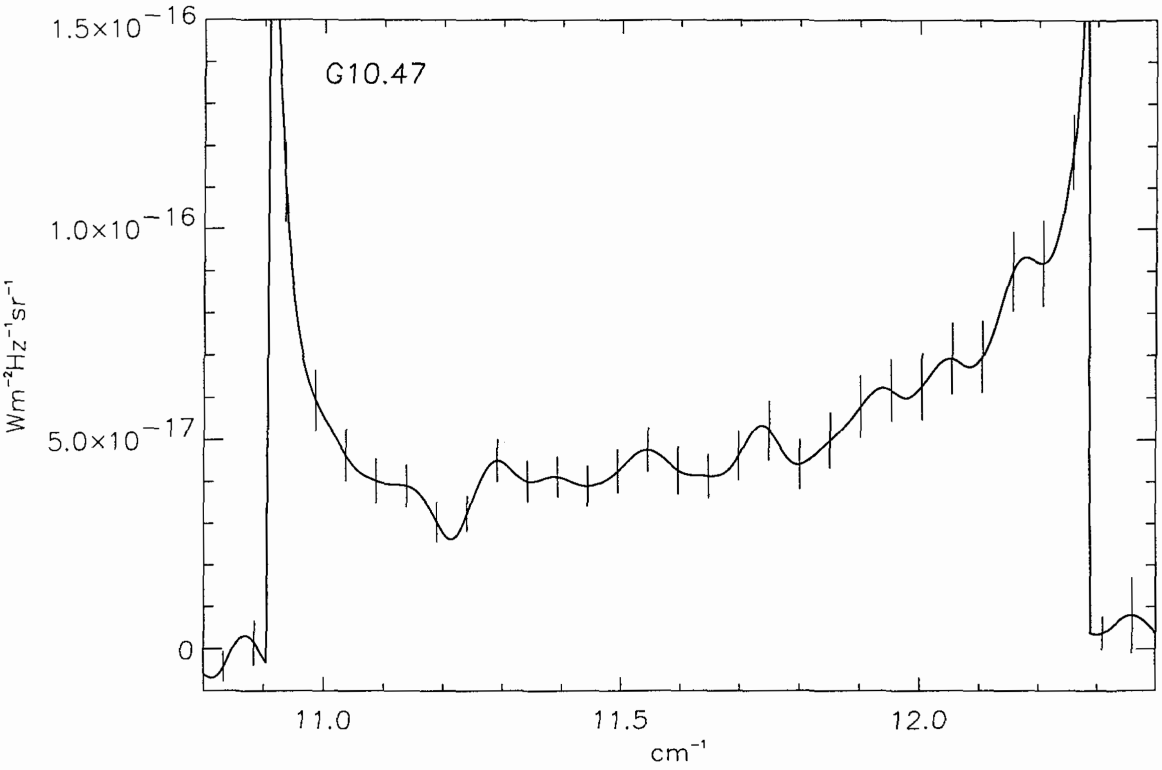

Figure 3.1 The final 850 μm low resolution spectrum of G10.47 with error bars at the 1σ level. The discontinuity is due to correcting the spectrum for transmission only within the band. The small peaks visible in the spectrum may be due to molecular line emission, such as CO (3-2) (11.53 cm^{-1}) and H_2CO (5_{15}-4_{14}) (11.73 cm^{-1}).

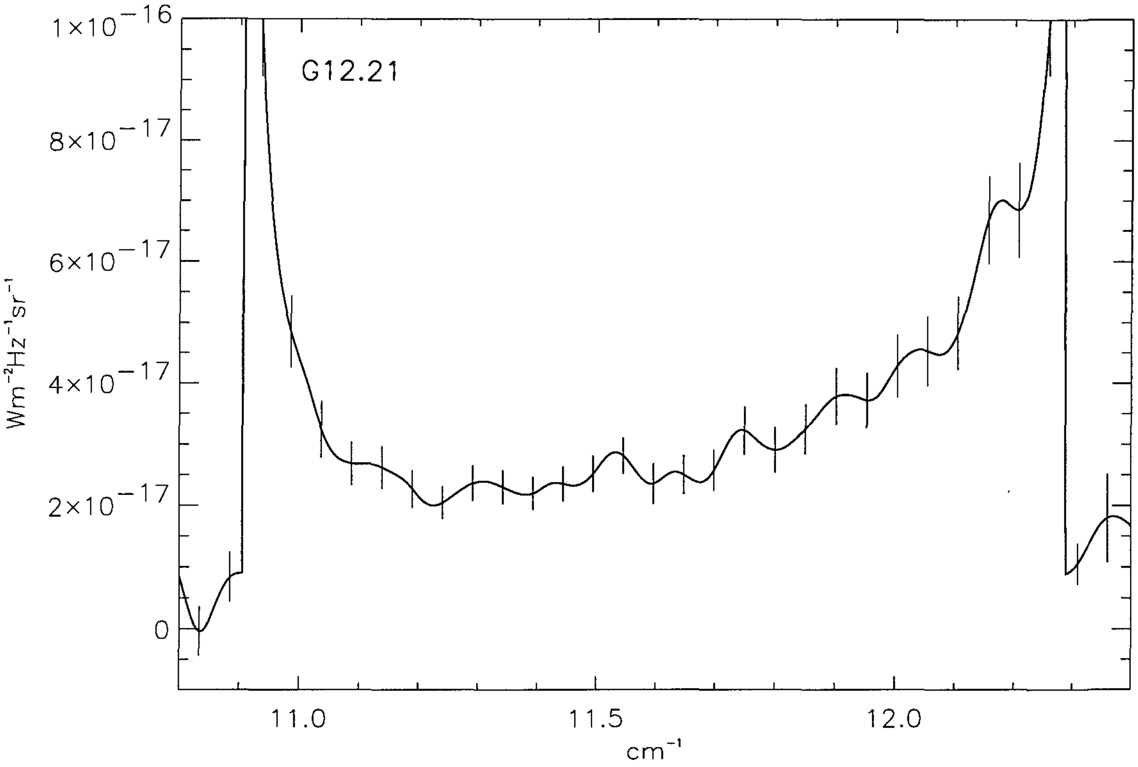

Figure 3.2 The final 850 μm low resolution spectrum of G12.21 with error bars at the 1σ level. The discontinuity is due to correcting the spectrum for transmission only within the band. The small peaks visible in the spectrum may be due to molecular line emission, such as CO (3-2) (11.53 cm^{-1}) and H_2CO (5_{15}-4_{14}) (11.73 cm^{-1}).

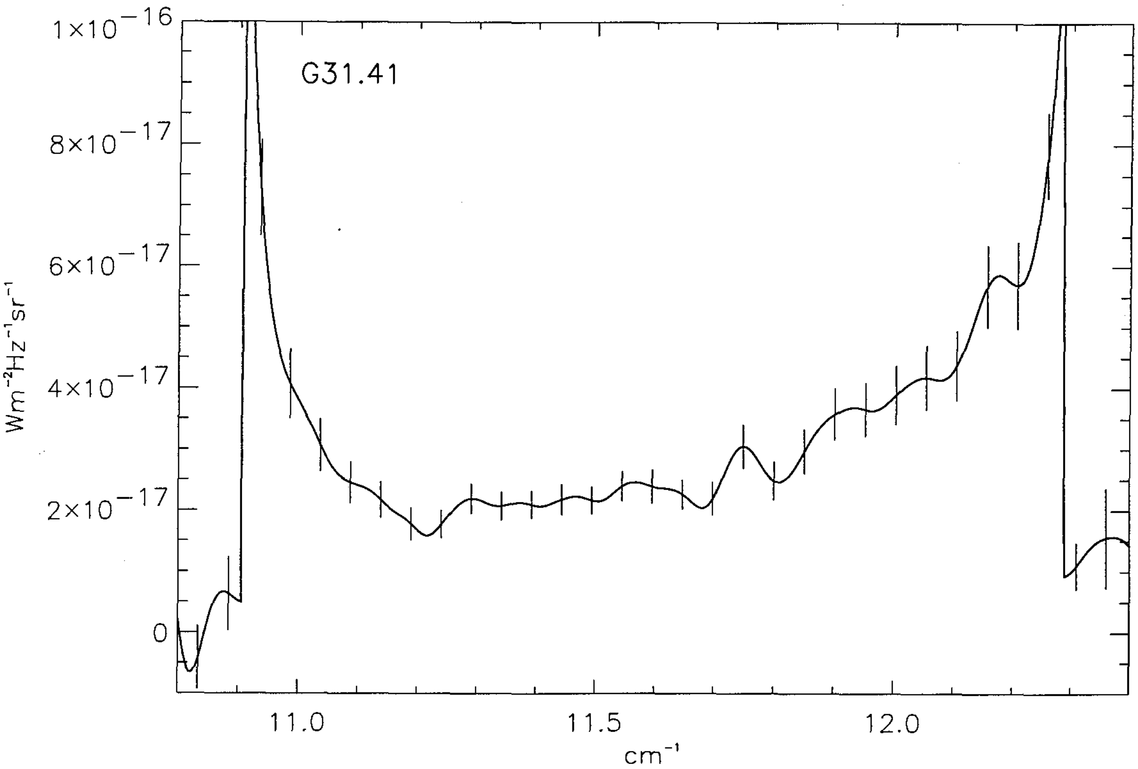

Figure 3.3 The final 850 μm low resolution spectrum of G31.41 with error bars at the 1-σ level. The discontinuity is due to correcting the spectrum for transmission only within the band. The peak at 11.73 cm^{-1} may be due to molecular line emission, such as $H_2CO(5_{15}\text{-}4_{14})$.

Table 3.1. Instrumental and observed S/N values

Object —	Time on source (hours)	S/N_{Ins} —	S/N_{Obs} —
G10.47	3.5	147	8.5
G12.21	4.0	73	7.4
G31.41	4.0	99	8.0

Note. — The instrumental and observed signal-to-noise ratio for each source.

S/N achieved across the band a factor of order $\sim$ 10 lower than the instrumental value for all sources. With all detector effects accounted for in the instrumental S/N, the sensitivity degradation is solely due to the atmospheric variance during our observations.

At submillimetre wavelengths, the brightness and variability of the sky is an overwhelming obstacle to accurate flux calibration, and observations generally require some form of chopping between source and background measurements in order to remove the sky emission. Ideally, the time between source and background measurements is as short as possible to limit the level of sky variance between observations (Archibald et al., 2002). While our observational method was designed to minimize the effects of the ever-changing atmosphere on the data by switching between source and background observations every 90 s, the atmosphere still contributed substantially to our uncertainties for several reasons. First, the opacity varies on timescales shorter than 90 s, as shown in Figure 2.6. Second, delays in slewing the telescope to the background position resulted in slight differences between the airmass of the background and source scans. For example, observing the background at a slightly larger airmass than the source effectively increases the opacity in the background scan relative to the on-source scan. In the submillimetre, the atmospheric opacity is dominated by absorption by H_2O, O_2 and O_3. As a quick test, we can think of a small increase in opacity as a small increase in the precipitable water vapour (with the caveat that there are other contributions to the opacity). Using atmospheric emissivities calculated for various pwv levels with ULTRAM, we have calculated that a modest jump in pwv of 0.1 mm, very reasonable when combining small deviations between source and background airmass with actual changes in the atmospheric pwv levels, increases the atmospheric emission by $\sim 40\,\mathrm{Jy}/14''$ beam at $850\,\mu$m. The pwv values calculated from the CSO τ_{225} for the observations contain jumps of this size, as shown in Figure 2.3. For this reason, stable weather is more crucial to this study than particularly good weather. A change in atmospheric emission of 40Jy is comparable to the flux of our brightest source, G10.47, and brighter than the others (see Table 2.1). As a consequence, some of the subtractions of the source and background spectra resulted in unphysical, negative flux measurements, while others resulted in impossibly high source brightnesses. When the spectra are coadded, however, on the whole these overly positive and negative scans will average out unless there is a large systematic offset between source and background observations or the pwv levels in the atmosphere are systematically increasing or decreasing. While there was a small systematic offset in the airmass between the on- and off-source scans, it was not large enough to produce significant changes in the sky emission except in the case of G31.41, which was observed while setting. For this source, the offset decreased the observed flux by at most 1-2 Jy/beam. During observations the changes in the atmospheric opacity were not consistently positive or negative.

Additionally, we argue that the atmospheric variance, while degrading our final S/N compared to the instrumental S/N, does not significantly affect the determination of the slope of the continuum emission. At low resolution, changes in atmospheric emission are essentially constant across the bandpass for small changes in the precipitable water vapour levels. This effect is illustrated in Figure 3.4, where the changes in atmospheric emissivity for several different values of the pwv are plotted at our observational resolution against the final standard deviation per data point of G10.47. For small jumps in the atmospheric pwv levels ($\leq$0.5 mm), the change in atmospheric emission is essentially constant within the region of interest. This implies that while the variable atmosphere may certainly affect the observed intensity of a source, it has less of an effect on the slope of the emission if the atmospheric changes are relatively small, as we would expect for our short observation times. The final observed S/N are remarkably constant across the band, with average deviations from the mean S/N values listed in Table 3.1 of only ±0.6. The standard deviation per point of the G10.47 data increases where the change in atmospheric emissivity is larger for even small jumps in the pwv levels, showing that the uncertainty in the data points is linked to the atmospheric variance.

3.3 Signal strength

The final flux values recorded for each source by the FTS are listed in Table 3.2 with calculated uncertainties. From Equation 3.5, we see that the uncertainty in the final flux value comes from the uncertainty in the observed flux $S_s(\nu)$, the uncertainty in the telescope coupling η_a, and the uncertainty in the atmospheric transmission, $\mathrm{e}^{-\tau(\nu)}$. The uncertainties in the gain G and the FTS response $R(\nu)$ are negligible compared to the other factors. From the S/N of the observations, the uncertainty in $S_s(\nu)$ is $\sim$ 11 – 12% for the three brightest sources. We take an uncertainty in η_a of 10%, and an uncertainty in the atmospheric transmission of 10%. Added in quadrature, this gives an uncertainty in the calibrated source flux of 20%. Additionally, the error lobe of the 850 μm JCMT beam may contain up to $\sim$ 5% of

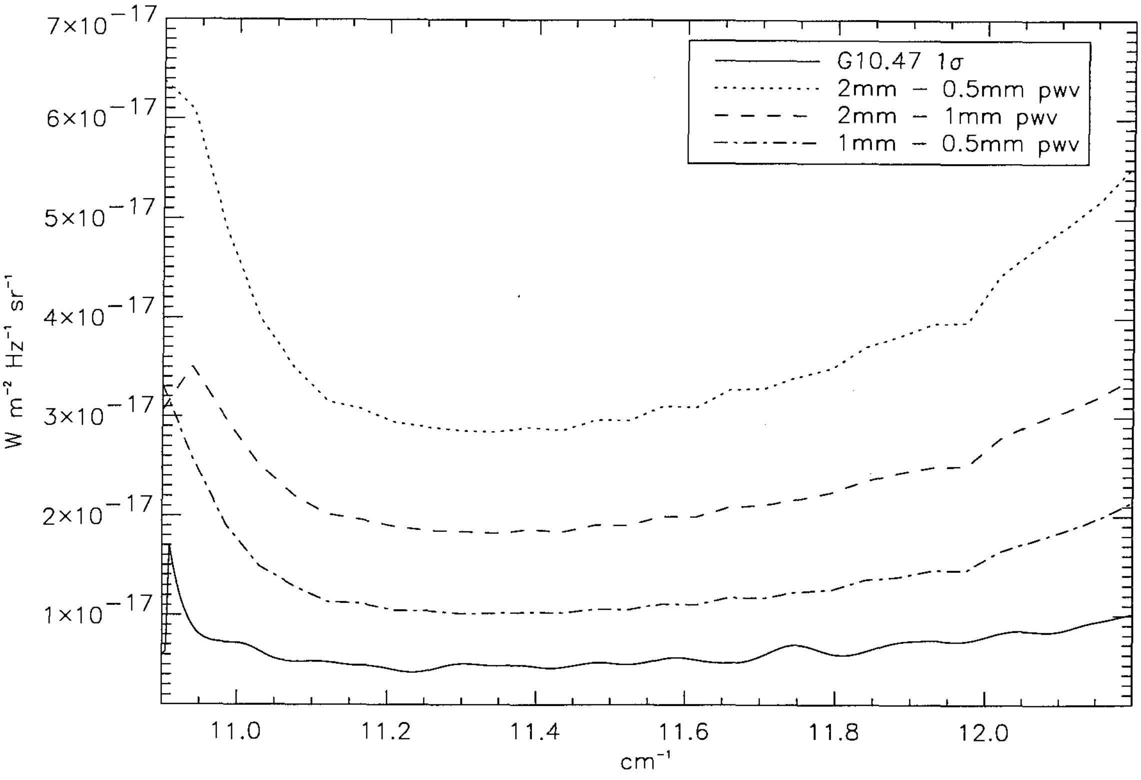

Figure 3.4 Changes in atmospheric emissivity due to changes in the precipitable water vapour levels compared to the 1σ standard deviation of the G10.47 data. The differences in the atmospheric emissivity have been calculated for different precipitable water vapour values using ULTRAM, and have all been scaled down by a factor of 50 for comparison with the standard deviation per point of the G10.47 data.

the source flux, making the final uncertainties of order 25%.

The final average brightnesses across the band are near those recorded for these sources by SCUBA, but are not within uncertainties for G10.47 or G31.41. There are several reasons why this may be the case. First, the calibration was done using a beam-filling blackbody placed in one input port of the FTS. While this is a complete detector calibrator, it does not account for the losses as the beam travels through the telescope, which we have attempted to address using the telescope efficiency for a similarly-placed instrument, SCUBA. Second, the coupling efficiency of the beam to our FTS detector aperture is less than 100%. Third, the discrepancies may also be due to poor atmospheric subtraction, as discussed in the previous section. These factors can easily account for the the discrepancies between the brightness values recorded by SCUBA and the FTS.

3.4 Molecular line contamination

The sources observed in this study are hot molecular cores. The warm temperatures of these objects, likely heated by some internal mechanism such as the emission from an embedded young star or cluster of stars, cause molecules and elements frozen onto the surface of dust grains during the colder collapse phase to evaporate, releasing these species into the gas phase where they can then be detected in emission lines. The observed emission lines are often from species excited at high temperatures and densities. HMC are thus characterized observationally by small diameters ($\lesssim$0.1 pc), high densities ($\gtrsim 10^7\,\mathrm{cm}^{-3}$), and warm temperatures ($\gtrsim$100 K) (Kurtz et al., 2000), and are often associated with other indicators of ongoing star formation, such as UCH II regions and masers. The sources in this study have been detected in many molecular lines (Hatchell et al., 1998) from multiple species present in the 850 μm atmospheric window.

At our low spectral resolution, only very bright, relatively broad lines would

Table 3.2. Comparison of source brightnesses from SCUBA and the FTS

Object	I_ν (SCUBA)	I_ν (FTS)
—	Jy/14″ beam	Jy/14″ beam
G10.47	39.0 ± 5.9	27 ± 6.8
G12.21	13.0 ± 2.0	16 ± 4.0
G31.41	24.2 ± 3.6	15 ± 3.8

Note. — A comparison of the 850 μm source brightnesses determined using the FTS with the peak brightnesses recorded by the Submillimeter Common User Bolometer Array. The fluxes are listed in Jy/14″ beam. The uncertainties in the SCUBA fluxes are 15%, while the uncertainties in the FTS fluxes are 25%.

contribute noticeably to the dust continuum spectrum. Our spectra show little evidence of bright line contamination. There is some evidence of small peaks in all the spectra, one of which appears to be at the CO(3-2) transition frequency; however the data do not allow a conclusive identification. The peaks are small and are not large enough to influence the continuum slope. The contamination of the continuum spectrum by single bright emission lines is therefore not a problem for this analysis, and the concern for this study is then the contamination of the continuum spectrum by a significant number of low-level emission lines that may be present and are not immediately visible, but which may influence the slope of the continuum.

The frequency coverage of molecular line studies for these sources is much less than that covered by the SCUBA detector and the FTS, so no absolute estimates of the level of contamination have been made (Hatchell et al., 2000). The contamination of the submillimetre continuum of hot core sources by molecular lines can range between 10% and (in extreme cases) 60% of the total integrated flux (Groesbeck et al., 1994). Johnstone et al. (2003) find that the 850 μm continuum emission from their observed protostellar sources, however, is never dominated by molecules other than CO (although line emission from HCN, HNC, CN and CH_3OH can contribute a substantial fraction of the contamination for more energetic sources) and line contamination in general is typically less than $\sim$ 10% at 850 μm, even for photon-dominated regions. The hot core regions of the sources observed in this study amount to a small fraction of the 850 μm beam (1-2$''$ compared with 14$''$), whereas the more extended emission is from cooler material in which fewer molecules will be excited. Overall, we argue that molecular line contamination of our low resolution 850 μm continuum is minimal, and does not significantly affect the analysis. We recognize, however, that it is important to consider the influence of these low-level molecular lines when making any determination of the slope of the dust continuum emission using low resolution submillimetre observations.

Chapter 4

Spectral Index Results and Interpretation

4.1 Calculation of the spectral index

From Equation 1.1, the dust emission $S(\nu) \propto \nu^{\gamma}$, where $\gamma = \beta + \alpha$ is the sum of the dust spectral index β and the frequency dependence α from the Planck function. For small ranges in frequency, we can expand this relationship:

$$\begin{aligned} S(\nu + \Delta\nu) &\propto (\nu + \Delta\nu)^{\gamma} \\ &\propto \nu_0^{\gamma}\left(1 + \gamma\frac{\Delta\nu}{\nu_0}\right) \end{aligned} \tag{4.1}$$

Thus, for small $\Delta\nu/\nu_0$, the dust emission is expected to increase linearly with frequency. The FTS passband at $850\,\mu$m is $\simeq 30\,$GHz wide, or $\simeq 10\%$ of the observing frequency, making the approximation valid. In practice, this window was made slightly smaller due to a decrease in S/N caused by increased levels of contaminating atmospheric flux near the edges of the band, leaving $\Delta\nu/\nu \simeq 0.07$ on average. A χ^2 minimizing linear fit routine was used to determine the slope of the continuum emission inside the passband. The analysis was done with and without apodizing the interferograms before Fourier transformation of the data collected by the FTS.

Apodization did not significantly affect the uncertainty per data point, likely because changes in the atmosphere, as described earlier, mainly contributed an upward or downward shift to the continuum flux which would not be substantially affected by apodization. The effect of apodization on the analysis was twofold: it smoothed the data to the eye and, perhaps against intuition, increased the uncertainty in the determination of β. Figure 4.1 shows the final spectrum for G10.47 determined using five different apodization functions of various strengths plotted against the final unapodized spectrum. The increased uncertainty in the slope fit is likely caused by the bleeding of the higher noise flux of the emission peaks near the edges of the band into the emission troughs by the smoothing function, as is evident in the Figure. The overall effect increases the apparent continuum, as well as the error bars, at the edges of the fitting window and thus influences the best continuum slope fit and reduces the size of the trustworthy fitting window. Apodization functions must therefore be used with care when studying continuum emission using this technique. All results quoted here have been determined from the unapodized data to ensure the greatest accuracy. The results varied slightly depending on the fraction of the band used (due to increasing error bars at the band edges when using more of the band, and conversely due to a smaller lever arm when using less of the band); however any variations were within uncertainties.

Column 2 of Table 4.1 shows the best fit continuum emission slope γ for each source with uncertainties determined through the χ^2 fitting routine. The average reduced χ^2 value for the fits was ~ 0.6, indicating a very good fit to the data within the band. We expect, for a good linear fit, that the reduced χ^2 should be close to 1 for a sufficiently large number of data points. The small values of the reduced χ^2 in our fits suggest that the uncertainty per data point has been overestimated by $\sim 20\%$ for each source. Since, in χ^2 fitting, the uncertainty in the calculated slope varies as the uncertainty per data point, this implies that the uncertainties in our slopes are also overestimated by 20%.

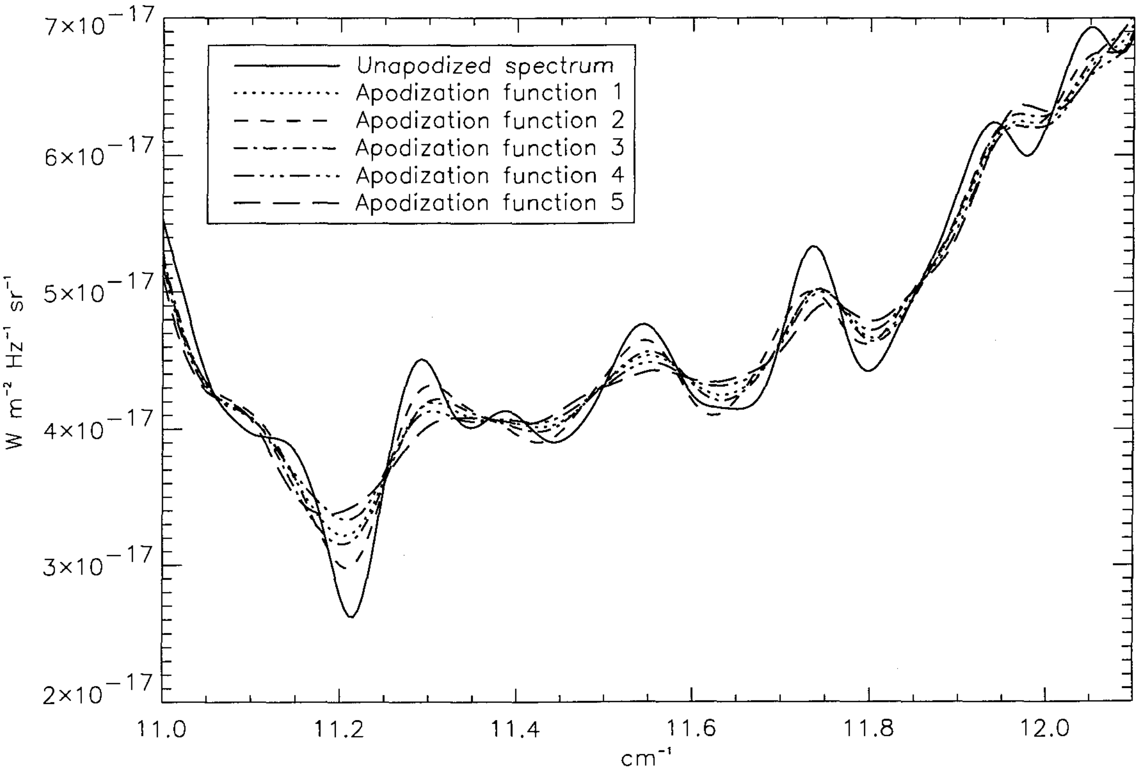

Figure 4.1 The final spectrum for the source G10.47, unapodized and calculated using several different apodization functions:

Apodization function 1: $1 - x/L$

Apodization function 2: $1 - (x/L)^2$

Apodization function 3: $(1 - (x/L)^2)^2$

Apodization function 4: e^{-x^2/L^2}

Apodization function 5: $0.355765 + 0.487395\cos(\pi x/L) + 0.144234\cos(2\pi x/L) + 0.012605\cos(3\pi x/L)$

L is the length of the one-sided portion of an interferogram in sample numbers. It is clear that the apodized spectra smooth over peaks in the unapodized spectrum, with the effect that the apodized continuum appears to have a greater slope near the edges of the band than the unapodized continuum.

For emission in the Rayleigh-Jeans limit, $\alpha = 2$ and thus $\beta = \gamma - 2$. In order for the R-J approximation to apply, $h\nu/kT \ll 1$, so $T \gg h\nu/k \sim 17\,\mathrm{K}$ at $850\,\mu$m. Modelling of the emission from these sources done by Hatchell et al. (2000) suggests that although the hot cores are surrounded by a shell of cold dust, the beam-averaged dust temperatures are high. For UC H II regions in general, the average dust temperature $T_d \sim 40 \pm 10\,\mathrm{K}$ (Hunter, 1998). In this case, the $850\,\mu$m emission is certainly in the R-J limit. Column 3 of Table 4.1 lists the dust spectral index β calculated for each source.

Figures 4.2-4.4 for each source show the final spectrum overlaid with the best linear fit.

4.2 Comparison with SCUBA data

The spectral index of dust emission can also be calculated using observations at two widely separated wavelengths. From Equation 1.1, we see that we can solve for $\gamma = \beta + \alpha$ with a ratio of the flux at two different wavelengths:

$$\gamma = \frac{\ln(S_2\,/\,S_1)}{\ln(\nu_2\,/\,\nu_1)} = \beta + \alpha \tag{4.2}$$

For our sources, archived SCUBA data at 450 μm and 850 μm is available. In order to properly compare the flux at the two wavelengths, the $8''$ resolution 450 μm data was first convolved to the resolution of the 850 μm data. The ratio of the peak brightnesses were then used to calculate γ from Equation 4.2. Column 4 of Table 4.1 gives the γ value calculated from the ratio of the $450\,\mu$m and $850\,\mu$m fluxes for each source. The uncertainties in this calculation are dominated by the uncertainty in the source flux at both wavelengths.

If the R-J approximation applies at both frequencies ν_1 and ν_2, then $\alpha = 2$ and $\beta = \gamma - 2$. As shown previously, the emission at $850\,\mu$m is likely in the R-J limit, but for the R-J approximation to apply at $450\,\mu$m, $T_d \gg h\nu/k \sim 32\,\mathrm{K}$. For the

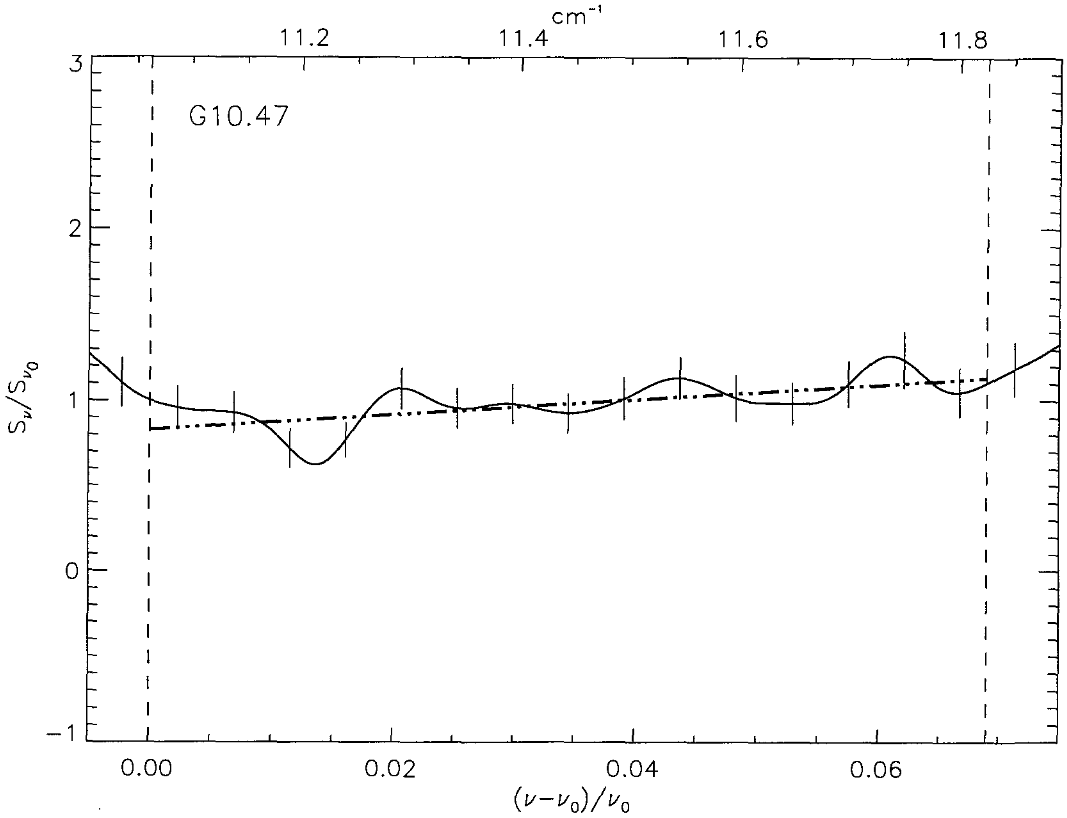

Figure 4.2 Final unapodized spectrum of G10.47 with 1σ error bars at 0.05 cm^{-1} resolution. The vertical dashed lines indicate the width of the fitting window. The dash-dotted line is the best fit linear slope.

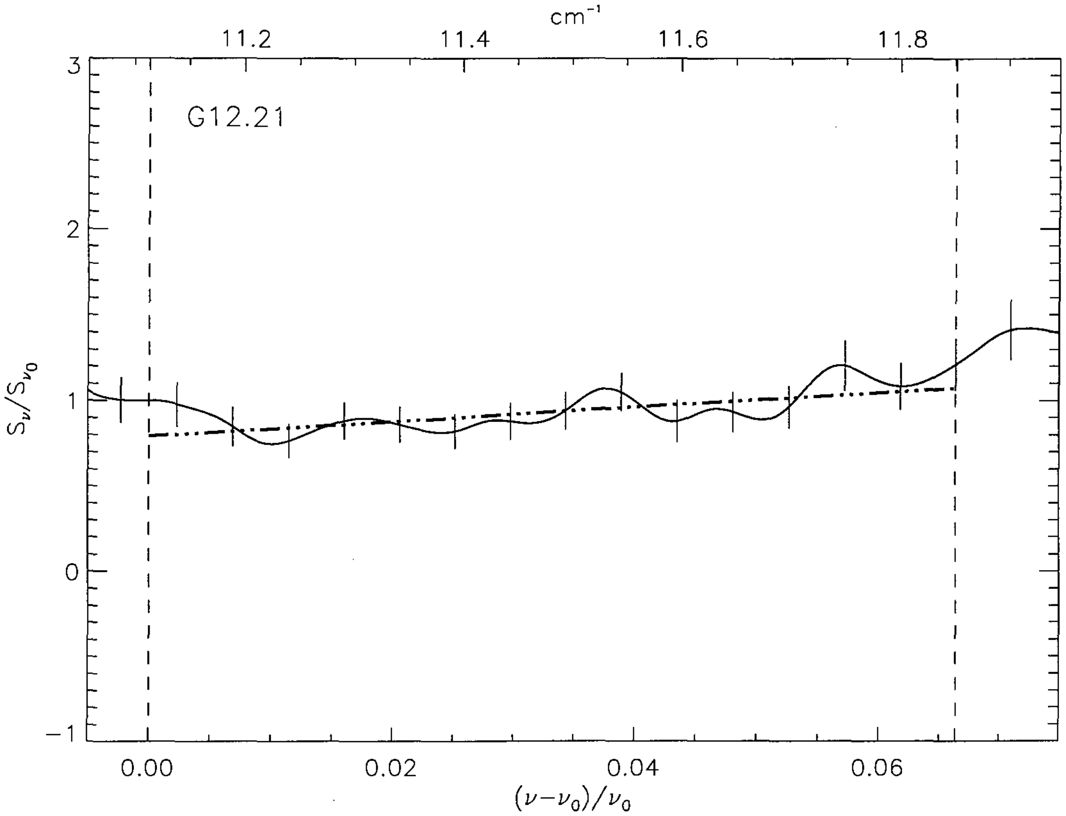

Figure 4.3 Final unapodized spectrum of G12.21 with 1σ error bars at $0.05\,\mathrm{cm}^{-1}$ resolution. The vertical dashed lines indicate the width of the fitting window. The dash-dotted line is the best fit linear slope.

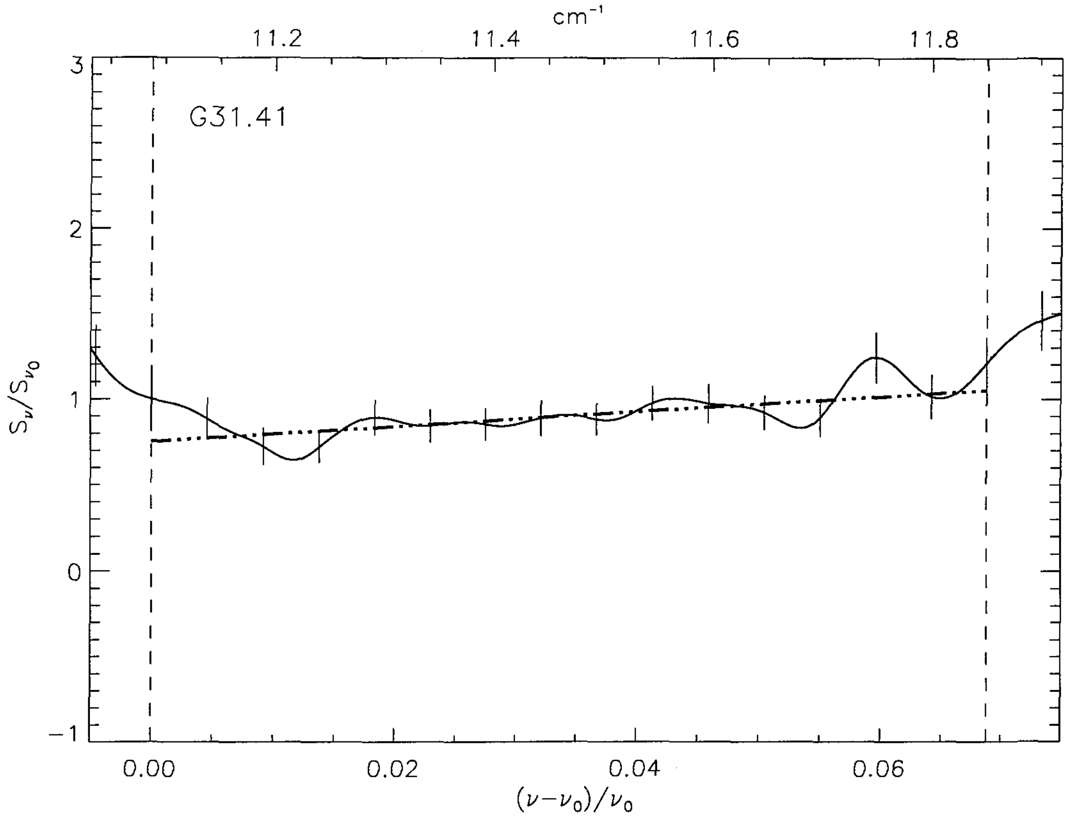

Figure 4.4 Final unapodized spectrum of G31.41 with 1σ error bars at $0.05\,\mathrm{cm}^{-1}$ resolution. The vertical dashed lines indicate the width of the fitting window. The dash-dotted line is the best fit linear slope.

average dust temperatures likely associated with these hot molecular core sources, the 450 μm emission cannot be assumed to be in the R-J limit. At lower temperatures, we find that $\alpha < 2$. If Equation 4.2 is used in determining β, assuming $\alpha = 2$ for sources with emission not in the R-J limit, a correction must be made to the calculated β which is dependent on the average dust temperature of the source, T_d (Goldsmith et al., 1997):

$$\Delta\beta = \frac{\ln\left[(\mathrm{e}^{T_2^*/T_d} - 1)/(\mathrm{e}^{T_1^*/T_d} - 1)\right]}{\ln T_2^*/T_1^*} - 1 \qquad (4.3)$$

Here, $T_1^* = h\nu_1/k$ and $T_2^* = h\nu_2/k$.

Combining the archived 450 μm and 850 μm SCUBA data with the submillimetre continuum slope determined using the FTS, it is possible to independently calculate both the dust spectral index and the average dust temperature of the sources. From Table 4.1, it is clear that the spectral indices calculated for two sources, G10.47 and G31.41, assuming $\alpha = 2$, are not consistent with the spectral index of the dust emission determined using the FTS (although the values determined are within uncertainties). These results require a β correction of order $\Delta\beta \sim 0.8$ in order to exactly match β determined using the FTS. From this correction, Equation 4.3 indicates that the average dust temperature of these two sources is $T_d \leq 20\,\mathrm{K}$, colder than results from Hunter (1998) for HMC in general. A β correction of $\Delta\beta \sim 0.5$, however, for these sources ensures the spectral indices calculated with the different methods are within uncertainties of each other, and indicates an average dust temperature of $T_d = 30\,\mathrm{K}$, consistent with Hunter (1998). G12.21, with $\gamma = 4.2$ from the ratio of fluxes, must have $\Delta\beta \simeq 0.2$, indicating an average dust temperature for the region of $T_d \simeq 60\,\mathrm{K}$. These results are listed in the final two columns of Table 4.1.

After completion of this thesis, a new method of calibration through observations of an astronomical blackbody source, the planet Mars, was attempted. The flux of the astronomical blackbody travels through the same optics as the flux from the HMC sources, and thus is a more reliable calibrator than the blackbodies placed

Table 4.1. Spectral indices and average dust temperatures

Source	γ	β	γ_{SCUBA}	$\Delta\beta$	T_d (K)
G10.47	4.3 ± 1.2	2.3 ± 1.2	3.5 ± 0.6	0.8	≤ 20
G12.21	4.4 ± 1.1	2.4 ± 1.1	4.2 ± 0.6	≤ 0.2	≥ 60
G31.41	4.3 ± 1.2	2.3 ± 1.2	3.4 ± 0.6	0.9	≤ 20

Note. — Spectral indices of three hot molecular cores determined from FTS and multiple wavelength observations. Column 2 shows the best slope from the χ^2 linear fit to the continuum FTS data. Column 3 lists the resulting β assuming that the emission at 850 μm is in the Rayleigh-Jeans limit. Column 4 gives the spectral indices of the sources calculated from the ratio of the 450 μm and 850 μm fluxes, and Columns 5 and 6 list the β-correction required and the consequent average dust temperatures T_d of the sources.

in the input port of the FTS. Additionally, the response of the detector to a very extended blackbody (such as that placed in the input port for this study) differs from its response to Mars, which was resolved. This calibration will be included in the journal article on this study, submitted soon after the completion of this thesis.

4.3 Interpretation

These results are consistent with the values of β found in embedded UC H II regions and other HMC. Fitting models of HMC to observational data have found $\beta = 1.6 - 2$ (Osorio et al., 1999; Churchwell et al., 1990). In a study of 17 UC H II regions, Hunter (1998) finds an average spectral index of $\beta = 2.0 \pm 0.25$ through greybody modelling of IRAS, submillimetre and millimetre observations. Observations and modelling of six compact HII regions, one of which was G10.47, by Hoare et al. (1991) find an average $\beta \simeq 1.5$. They note, however, that the frequency dependence is somewhat affected by the assumed density distribution of the model. The dense ridge in Orion has $\beta \simeq 1.9$ near embedded infrared sources (Goldsmith et al., 1997). Overall, the spectral indices of these warmer, likely more evolved star forming regions tend to be higher than those found in cooler, less evolved dense cores, indicating that dust properties have changed through some mechanism which appears to correlate with protostellar age.

Several dust models predict a dust opacity frequency dependence similar to that found here, but our observations are not sensitive enough to determine a most likely dust composition. Higher values of β have been associated with dust grains covered in thick ice mantles (Aannestad, 1975; Lis and Menten, 1998), while many dust grain models with combinations of silicate and graphite compositions find a spectral index of $\beta \sim 1.5 - 2$.

While we had hoped to determine γ to an accuracy of ± 0.1, the variable atmosphere at $850\,\mu$m degraded the achieved signal-to-noise ratio by a factor $\gtrsim 10$

compared with the instrumental S/N, leading to uncertainties in our calculation of β of approximately ± 1.1. Even with the atmospheric problems, however, the uncertainties determined here are of the same order as those found when calculating the dust spectral index through multiple wavelength observations of single sources. These results show that with better sky subtraction techniques, it should be easily possible to determine the spectral index of bright astronomical sources with high accuracy using an FTS. Future instruments with greater sensitivity and precise sky subtraction will enable the measurement of spectral indices of much fainter sources. Careful sky subtraction is *essential* to future studies of the continuum emission with an FTS.

Chapter 5

Future prospects

5.1 SCUBA-2

The Submillimetre Common User Bolometer Array (SCUBA) (Holland et al., 1999) at the JCMT is a submillimetre detector array, containing 37 pixels at longer wavelengths (750 μm - 1350 μm) and 91 pixels at shorter wavelengths (350 μm - 450 μm) in a hexagonal pattern. It was designed to replace the single bolometer detector, UKT14, at the JCMT, and was revolutionary in its high sensitivity, large wavelength range and dual-wavelength mapping capability. SCUBA has had an immense impact on astronomy. A study by Georges Meylan from the Space Telescope Science Institute in 1999 showed that the number of citations from SCUBA papers was second only to those from the Hubble Space Telescope. While SCUBA has revolutionized submillimetre astronomy, it is limited by the small size of its pixel arrays and by the difficulties in atmospheric correction at these wavelengths. As a result, mapping large areas of sky, or imaging regions deeply, is very time consuming. SCUBA-2[1] is the next generation submillimetre detector currently in development to

---

[1] SCUBA-2 is a collaboration between the UK Astronomy Technology Centre (Edinburgh), the National Institute of Standards and Technology (Boulder), the Scottish Microelectronics Centre (Edinburgh), the University of Wales (Cardiff), and the Joint Astronomy Centre (Hawaii). SCUBA 2 is a jointly funded project through the JCMT Development Fund with substantial additional con-

replace the SCUBA detector at the JCMT in late 2005 (Holland et al., 2003). The SCUBA-2 detector will utilize over 12,000 pixels in two arrays, enabling imaging in both the 450 μm and 850 μm bands simultaneously and making CCD-style imaging in the submillimetre a reality. The instrument will have a field of view $8'$ in diameter, an increase in imaging area of $\gtrsim$10 times over the $2.3'$ diameter field of view of the existing SCUBA detector. The detectors are over ten times more sensitive than the current SCUBA bolometers, and this, combined with the greater field of view, will lead to mapping speeds up to $\sim$ 1000 times faster than with SCUBA. SCUBA-2 will be a pathfinder for new submillimetre and millimetre interferometers such as the Submillimetre Array and the Atacama Large Millimetre Array. A polarimeter and an imaging FTS (IFTS) will be combined with the imaging component of SCUBA-2, greatly enhancing the capabilities of this exciting new detector.

5.2 An IFTS for SCUBA-2

An imaging FTS has been chosen as a complementary instrument to SCUBA-2 (Naylor and Gom, 2004). Utilizing SCUBA-2's highly sensitive detector array, the IFTS will obtain simultaneous, variable spectral resolution 450 μm and 850 μm wavelength spectra at every pixel in its field of view, providing an unprecedented third dimension in submillimetre astronomical observations. This will enable the construction of detailed physical models of observed astronomical sources, with the morphological information obtained with SCUBA-2 complemented by knowledge of the physical and compositional conditions determined through submillimetre spectral analysis. The field of view is determined by the detector beamsplitter apertures, and at minimum two fields, each with a diameter of $3'$, are currently proposed. The IFTS will be useful for a variety of astronomical studies, including those of the interstellar medium and star forming regions, ultra-luminous infrared galaxies, and planetary atmospheres,

---

tributions from the UK Office of Science and Technology and the Canada Foundation for Innovation.

and is scheduled to be delivered to the JCMT in 2006.

The IFTS will use the Mach-Zehnder design of the FTS used in this study, enabling two input ports; one of which will view the source while the other will view an adjacent region of sky. With the second input port on the sky, the atmospheric emission can be subtracted from the astronomical source on an instantaneous, pixel-by-pixel basis, minimizing atmospheric noise contributions and potentially providing nearly detector-limited sensitivity, as well as a 100% increase in observing efficiency compared with the observations presented here. Based on detector noise calculations alone, the IFTS will be at least 10 times more sensitive per pixel than the single bolometer FTS used in these observations (Gom and Naylor, 2004). The extremely accurate sky subtraction possible with the IFTS will provide an even more substantial increase in the observational precision. When also considering the variable atmosphere noise, the sensitivity of the IFTS increases to at least 100 times greater than in the observations presented in this paper.

The permanent placement of the instrument on the telescope will allow IFTS users to take advantage of good weather to observe both short and long wavelength emission. This is a great benefit for studies of the spectral energy distribution of dust in star forming regions. In very good weather, measurements of the dust spectral index γ made at both the $450\,\mu$m and $850\,\mu$m wavelengths will allow the determination of both the dust temperature and the wavelength dependence of the dust opacity of a source, providing an accurate temperature and spectral index map of the observed region. This will eliminate the present ambiguity of interpreting differences in observed values of the dust spectral index as due to either dust evolution effects or the change in temperature across a source. With this instrument, it will be possible to make highly constrained comparisons between observations and dust composition models.

Using the detector sensitivities in Gom and Naylor (2004), we have calculated in Table 5.1 (through linear χ^2 fitting analysis) the source brightnesses required to determine the spectral index γ of submillimetre dust emission $\gamma = \beta + \alpha$ to ± 0.1 and

Table 5.1. Source brightnesses required to determine γ in 12 hours of observing

Wavelength μm	Resolution GHz	Resolution cm^{-1}	12 hrs 1-σ ΔT mK	Source brightness $\gamma \pm 0.1$ (Jy/beam)	Source brightness $\gamma \pm 0.3$ (Jy/beam)
450	3.0	0.1	1.44	4.7	1.6
850	3.0	0.1	0.2	0.40	0.14

Note. — Source brightnesses required to determine the dust spectral index γ in 12 hours of observing using an IFTS on SCUBA-2.

±0.3 accuracy in 12 hours of observing with the IFTS at the JCMT. At low resolution, it will be possible to determine γ, and hence β, with high precision of the dust emission from sources only 400 mJy/beam in brightness at 850 μm, and with somewhat less precision of sources only $\sim$ 140 mJy/beam in brightness, in a 12 hour observation. Using the imaging FTS, it will be possible to determine with high precision the dust properties *across* sources through the spectral information obtained in each pixel in the field of view.

Chapter 6

Summary

Knowledge of the physical parameters of star forming regions, such as mass, temperature and density distributions, allows the construction and evaluation of ever more detailed models of how stars form. Observations of the emission from dust in molecular clouds have proved highly beneficial to star formation studies, as many physical properties of the observed regions can be derived through analysis of the dust emission. These calculations are dependent, however, on the assumed physical parameters of the emitting dust. The composition, grain size distribution, and temperature of the dust all affect the observed submillimetre spectral energy distribution, with the result that changes in emissivity within clouds may stem from a drop in the average temperature of a region or from the evolution of the dust within the system. Given this ambiguity, the derived masses of regions determined through submillimetre observations often have large uncertainties, as the mass in particular depends heavily on the dust temperature and opacity. It is therefore desirable to find methods in which to determine dust properties unambiguously from observations.

The dust opacity is often modelled as having a power law dependence on frequency, with the calculated power law index $\beta \simeq 0 - 3$ dependent on the dust composition. Multiple wavelength observations, which display changes in the dust emissivity with wavelength, have found a similar range of values in molecular clouds and star forming regions, with evidence of dust evolution along with its environment.

We have determined the dust spectral index β of three hot molecular cores solely within one passband using an FTS on the JCMT. We find an average $\beta \simeq 2.3$, in agreement with β calculated for the same sources using observed submillimetre flux ratios and consistent with measurements of the spectral index in other HMCs. The uncertainties in β in these observations are dominated by the difficulties in subtracting the very bright and variable submillimetre atmosphere from the data, with the atmosphere degrading the sensitivity of the observations from the instrumental sensitivity by a factor of 10. With better sky subtraction techniques, as will be possible with an IFTS on SCUBA-2, these uncertainties will be greatly reduced.

The sensitivity of the IFTS planned for SCUBA-2 will be greater by a factor of $\sim$ 100 than that of the single pixel detector used in this study, and will allow the determination of the spectral index of dust emission of sources with brightnesses of only a few hundred mJy/JCMT beam. Combined with 450 μm data, it will be possible to determine independently both the temperature of the emitting dust and the frequency dependence of the emission. The IFTS is scheduled to be delivered to the JCMT in 2006.

Bibliography

Aannestad, P. A.: 1975, *Astrophys. J.* **200**, 30

Archibald, E. N., Jenness, T., Holland, W. S., Coulson, I. M., Jessop, N. E., Stevens, J. A., Robson, E. I., Tilanus, R. P. J., Duncan, W. D., and Lightfoot, J. F.: 2002, *M.N.R.A.S.* **336**, 1

Beckwith, S. V. W. and Sargent, A. I.: 1991, *Astrophys. J.* **381**, 250

Beuther, H., Schilke, P., and Wyrowski, F.: 2004, *Astrophys. J.* in press

Chapman, I.: 2000, *Master's thesis*, University of Lethbridge

Chapman, I. M., Naylor, D. A., and Phillips, R. R.: 2004, *M.N.R.A.S.* pp 364–+

Churchwell, E., Wolfire, M. G., and Wood, D. O. S.: 1990, *Astrophys. J.* **354**, 247

Davis, G. R., Naylor, D. A., Griffin, M. J., Clark, T. A., and Holland, W. S.: 1997, *Icarus* **130**, 387

Draine, B. T. and Lee, H. M.: 1984, *Astrophys. J.* **285**, 89

Goldsmith, P. F., Bergin, E. A., and Lis, D. C.: 1997, *Astrophys. J.* **491**, 615

Gom, B. G. and Naylor, D. A.: 2004, in *Astronomical Telescopes and Instrumentation. Proceedings of the SPIE, Volume 5498, (2004) in press.*, pp 1–18

Groesbeck, T. D., Phillips, T. G., and Blake, G. A.: 1994, *Astrophys. J. Supp.* **94**, 147

Hatchell, J., Fuller, G. A., Millar, T. J., Thompson, M. A., and Macdonald, G. H.: 2000, *Astron. & Astrophys.* **357**, 637

Hatchell, J., Thompson, M. A., Millar, T. J., and MacDonald, G. H.: 1998, *Astron. & Astrophys. Supp.* **133**, 29

Hildebrand, R. H.: 1983, *Quart. Jour. Royal Astron. Society* **24**, 267

Hoare, M. G., Roche, P. F., and Glencross, W. M.: 1991, *M.N.R.A.S.* **251**, 584

Hogerheijde, M. R. and Sandell, G.: 2000, *Astrophys. J.* **534**, 880

Holland, W. S., Duncan, W., Kelly, B. D., Irwin, K. D., Walton, A. J., Ade, P. A. R., and Robson, E. I.: 2003, in *Millimeter and Submillimeter Detectors for Astronomy. Edited by Phillips, Thomas G.; Zmuidzinas, Jonas. Proceedings of the SPIE, Volume 4855, pp. 1-18 (2003).*, pp 1–18

Holland, W. S., Robson, E. I., Gear, W. K., Cunningham, C. R., Lightfoot, J. F., Jenness, T., Ivison, R. J., Stevens, J. A., Ade, P. A. R., Griffin, M. J., Duncan, W. D., Murphy, J. A., and Naylor, D. A.: 1999, *M.N.R.A.S.* **303**, 659

Hunter, T. R.: 1998, *Pub. Astron. Soc. Pacific* **110**, 634

Johnstone, D. and Bally, J.: 1999, *Astrophys. J. Letters* **510**, L49

Johnstone, D., Boonman, A. M. S., and van Dishoeck, E. F.: 2003, *Astron. & Astrophys.* **412**, 157

Kurtz, S., Cesaroni, R., Churchwell, E., Hofner, P., and Walmsley, C. M.: 2000, *Protostars and Planets IV* pp 299–+

Lis, D. C. and Menten, K. M.: 1998, *Astrophys. J.* **507**, 794

Lis, D. C., Serabyn, E., Keene, J., Dowell, C. D., Benford, D. J., Phillips, T. G., Hunter, T. R., and Wang, N.: 1998, *Astrophys. J.* **509**, 299

Naylor, D. A., Davis, G. R., Gom, B. G., Clark, T. A., and Griffin, M. J.: 2000, *M.N.R.A.S.* **315**, 622

Naylor, D. A., Davis, G. R., Griffin, M. J., Clark, T. A., Gautier, D., and Marten, A.: 1994, *Astron. & Astrophys.* **291**, L51

Naylor, D. A. and Gom, B. G.: 2004, in *Imaging Spectrometry IX. Edited by Sylvia S. Shen; Paul E. Lewis. Proceedings of the SPIE, Volume 5159, pp. 91-101 (2004).*, pp 1–18

Naylor, D. A., Gom, B. G., Ade, P. A. R., and Davis, J. E.: 1999, *Review of Scientific Instruments* **70**, 4097

Naylor, D. A., Gom, B. G., Schofield, I., Tompkins, G., and Davis, G. R.: 2003, in *Millimeter and Submillimeter Detectors for Astronomy. Edited by Phillips, Thomas G.; Zmuidzinas, Jonas. Proceedings of the SPIE, Volume 4855, pp. 540-551 (2003).*, pp 540–551

Osorio, M., Lizano, S., and D'Alessio, P.: 1999, *Astrophys. J.* **525**, 808

Ossenkopf, V. and Henning, T.: 1994, *Astron. & Astrophys.* **291**, 943

Pollack, J. B., Hollenbach, D., Beckwith, S., Simonelli, D. P., Roush, T., and Fong, W.: 1994, *Astrophys. J.* **421**, 615

Serabyn, E. and Weisstein, E. W.: 1995, *Astrophys. J.* **451**, 238

Visser, A. E., Richer, J. S., Chandler, C. J., and Padman, R.: 1998, *M.N.R.A.S.* **301**, 585

Walsh, A. J., Macdonald, G. H., Alvey, N. D. S., Burton, M. G., and Lee, J.-K.: 2003, *Astron. & Astrophys.* **410**, 597

Williams, S. J., Fuller, G. A., and Sridharan, T. K.: 2004, *Astron. & Astrophys.* **417**, 115

Wood, D. O. S. and Churchwell, E.: 1989, *Astrophys. J. Supp.* **69**, 831